Quantum-Mechanical Condensed Matter Simulations with CRYSTAL

R. Dovesi,[1] A. Erba,[1,*] R. Orlando,[1] C.M. Zicovich-Wilson,[2] B. Civalleri,[1] L. Maschio,[1] M. Rérat,[3] S. Casassa,[1] J. Baima,[1] S. Salustro,[1] and B. Kirtman[4]

[1] *Dipartimento di Chimica, Università di Torino, Via Giuria 5, 10125 Torino, Italy*
[2] *Facultad de Ciencias, Universidad Autónoma del Estado de Morelos, Av. Universidad, 1001, Col. Chamilpa, 62209 Cuernavaca, Morelos, Mexico*
[3] *Equipe de Chimie Physique, IPREM UMR5254, Université de Pau et des Pays de l'Adour, 64000 Pau, France*
[4] *Department of Chemistry and Biochemistry, University of California, Santa Barbara, California 93106, USA*

(Dated: October 4, 2017)

The latest release of the CRYSTAL program for solid state quantum-mechanical *ab initio* simulations is presented. The program adopts atom-centered Gaussian-type functions as a basis set, which makes it possible to perform all-electron as well as pseudopotential calculations. Systems of any periodicity can be treated at the same level of accuracy (from 0D molecules, clusters and nanocrystals, to 1D polymers, helices, nanorods and nanotubes, to 2D monolayers and slab models for surfaces, to actual 3D bulk crystals), without any fictitious repetition along non-periodic directions for 0-2D systems. Density functional theory calculations can be performed with a variety of functionals belonging to several classes: local-density (LDA), generalized-gradient (GGA), meta-GGA, global hybrid, range-separated hybrid and self-consistent system-specific hybrid. In particular, hybrid functionals can be used at a modest computational cost, comparable to that of pure LDA and GGA formulations, because of the efficient implementation of exact non-local Fock exchange. Both translational and point-symmetry features are fully-exploited at all steps of the calculation, thus drastically reducing the corresponding computational cost. The various properties computed encompass electronic structure (including magnetic spin-polarized open-shell systems, electron density analysis), geometry (including full or constrained optimization, transition-state search), vibrational properties (frequencies, infrared and Raman intensities, phonon density of states), thermal properties (quasi-harmonic approximation), linear and non-linear optical properties (static and dynamic (hyper)polarizabilities), strain properties (elasticity, piezoelectricity, photoelasticity), electron transport properties (Boltzmann, transport across nanojunctions) as well as X-ray and inelastic neutron spectra. The program is distributed in serial, parallel and massively parallel versions. In this paper, the original developments that have been devised and implemented in the last four years (since the distribution of the previous public version, CRYSTAL14, occurred in December 2013) are described.

I. INTRODUCTION

Quantum-mechanical simulations based on the density-functional-theory (DFT) do represent an effective mean to the prediction and characterization at the atomistic scale of several properties of materials.[1–3] The detailed chemical and physical insight provided by first-principle theoretical simulations is increasingly acknowledged by a broad community so that the computational approach has recently become a standard complementary tool to the experimental characterization in many fields of research.

An obvious prerequisite to the effectiveness and popularity of quantum-mechanical simulations in a solid state context is the availability of general-purpose, numerically-robust, user-friendly, computationally-efficient programs. In this paper, the functionalities of one such program, namely CRYSTAL17, are illustrated. In particular, the new developments and improvements with respect to the previous major release of the program, CRYSTAL14,[4] are discussed into detail.

At variance with most other programs for solid state applications, in CRYSTAL use is made of atom-centered Gaussian-type functions as a basis set.[5] All-electron or valence-only basis sets with effective core pseudopotentials can be used. Both Hartree-Fock (HF) and DFT calculations can be performed. Systems periodic in one dimension (1D polymers, helices, nanotubes, nanorods), two dimensions (2D monolayers, slab models for surfaces) and three dimensions (3D bulk crystals and amorphous materials through a super-cell approach) can be treated. As a limit case, non-periodic molecular systems (0D molecules, clusters, fullerenes, nanocrystals) can also be studied at the same level of theory and with the same numerical accuracy. Closed-shell as well as spin-polarized systems can be investigated. Both translational invariance and point-symmetry are thoroughly exploited at all steps of the calculation.[6–8] A schematic overview of the features of CRYSTAL is given in Figure 1. The main new features of CRYSTAL17 are highlighted in the figure, summarized below, and discussed into detail in Section II.

The Direct Inversion of Invariant Subspace (DIIS) convergence accelerator has been implemented for the self-consistent-field (SCF) procedure and for first- and second-order Coupled-Perturbed-Hartree-Fock/Kohn-Sham (CPHF/KS) self-consistent procedures. The use of such a scheme is found to drastically reduce the required number of iterations to get convergence and is thus activated by default.

A fully-automated algorithm has been devised to com-

pute quasi-harmonic thermal properties of solids beyond the harmonic approximation. The quasi-harmonic approximation (QHA) takes into explicit account the dependence of vibration phonon frequencies on volume and allows to compute volume-dependent thermodynamic properties such as the thermal expansion coefficient, constant-pressure (versus constant-volume harmonic) thermodynamic functions, thermal dependence of bulk modulus, etc.

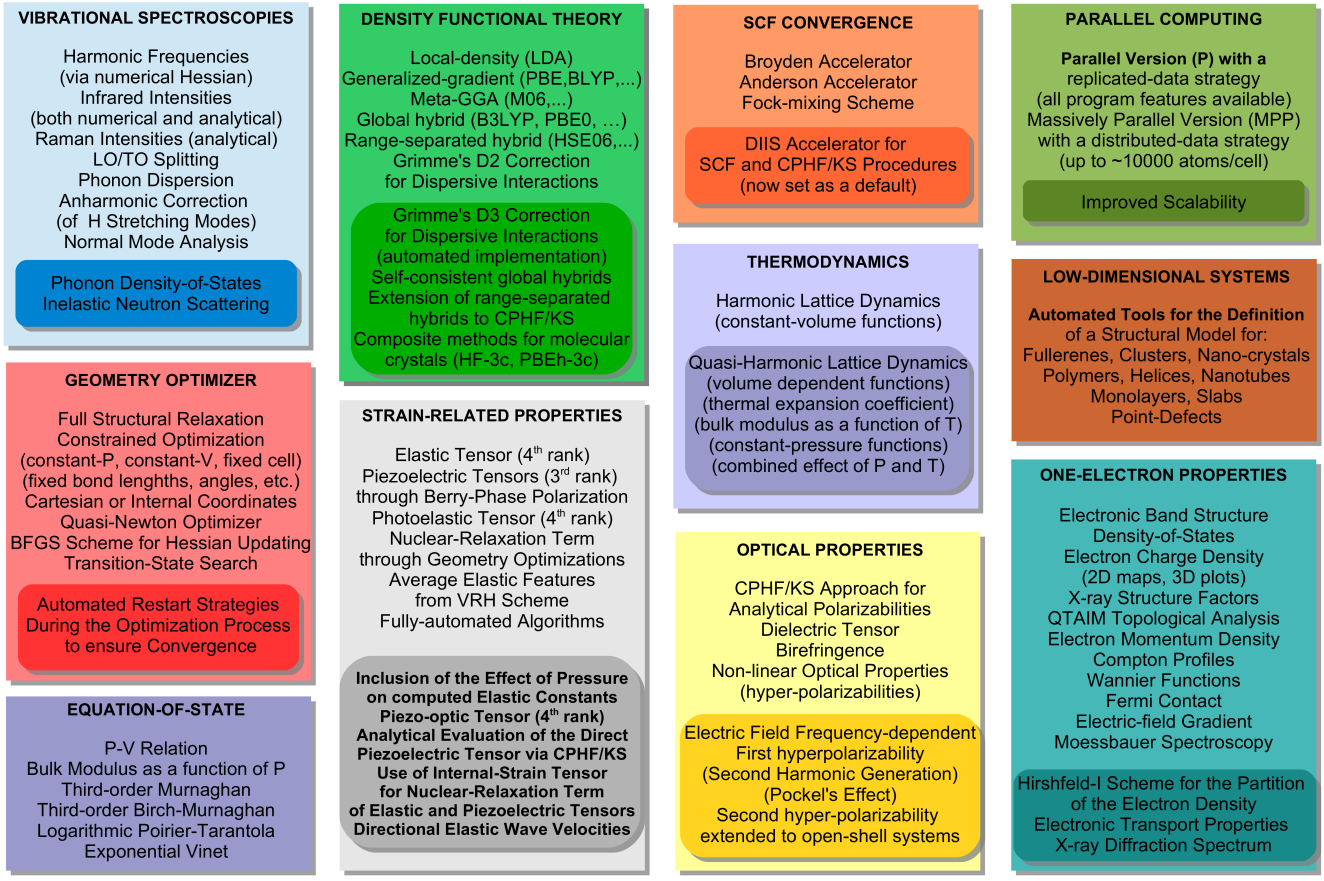

FIG. 1: Detailed list of features of the CRYSTAL program. For each topic, the new developments made in the CRYSTAL17 major release are highlighted in the darker boxes at the bottom.

A user-friendly (input parameter-free) implementation of Grimme's -D3 correction for the inclusion of weak dispersive interactions into DFT functionals has been made, which proves particularly suitable for the study of molecular, organic crystals and adsorption phenomena. The geometrical counterpoise (gCP) scheme to automatically correct for the basis-set-superposition-error (BSSE) in structural optimizations of molecular organic crystals has also been implemented. By combining the -D3 and gCP corrections, the newly-proposed composite HF-3c and PBEh-3c methods have been made available specifically targeted to molecular crystals.

The extension of first-order CPHF/KS equations to the description of dynamic (i.e. electric field frequency-dependent) polarizabilities and first-hyperpolarizabilities has been achieved, which makes it possible to simulate the second harmonic generation (SHG) and Pockels tensors.

New algorithms for the description of strain-related properties of materials have been devised allowing for: i) the calculation of the fourth-rank elastic tensor (and derived elastic properties) under pressure; ii) a thorough characterization of the anisotropic distribution of phase and group acoustic wave velocities, as well as of the related power flow angles and enhancement factors; iii) the analytical evaluation of the direct piezoelectric ten-

sor through a CPHF/KS approach; iv) the evaluation of the nuclear-relaxation term of elastic and piezoelectric tensors through the internal-strain tensor rather than through numerical geometry optimizations of atomic positions at strained configurations; v) the calculation of the piezo-optic tensor of crystals of any symmetry, which measures the variation of the dielectric response induced by an external stress.

One of the peculiar features of the CRYSTAL program is given by the high computational efficiency with which hybrid functionals (i.e. including a fraction of exact non-local HF exchange) of the DFT are treated. Hybrid calculations in the CRYSTAL program are only 2-3 times more computationally demanding than pure DFT ones both in terms of time and memory occupancy. A new family of hybrid functionals has been implemented: self-consistent hybrids, where a system-specific optimal fraction of exact exchange is automatically defined as inversely proportional to the dielectric response of the system. The applicability of a bunch of range-separated hybrid functionals has also been extended to CPHF/KS calculations.

The CRYSTAL program can be run in sequential mode and in two parallel modes: a replicated-data parallel one and a distributed-data massively-parallel one. The latest improvements as regards parallel scalability are discussed and an overview is presented of recent studies where the parallel versions of the program are used to study large systems in an effort to try to extend the applicability domain of DFT simulations for solids to more complex and possibly more realistic structural models.

The Hirshfeld-I partitioning scheme for the electron charge density has been implemented, which provides a further measure of atomic charges with respect to the previously available Mulliken, Born and Bader approaches. The X-ray diffraction spectrum can also be computed.

Total and atom-projected vibrational densities-of-states can now be computed both from a Γ-only vibration frequency calculation (to be used for large cell systems) and from a phono-dispersion calculation. The neutron-weighted phonon density-of-state is also computed, which can be compared to inelastic-neutron-scattering (INS) spectra.

Algorithms have been developed for the calculation of some electronic transport properties (such as the electronic conductivity, the Seebeck effect, the electronic contribution to the thermal conductivity) according to Boltzmann's semiclassical transport theory.

II. NEW FEATURES

A. DIIS for Improved SCF and CPHF/KS Convergence

The Direct Inversion of Invariant Subspace (DIIS) is a powerful technique to accelerate the SCF convergence. Initially proposed by Pulay in 1984,[9,10] it gained considerable reputation during the last 30 years. In previous versions of the CRYSTAL code, a Fock matrix damping, in conjunction possibly with eigenvalue shifting, was used as a default. Modified Broyden[11] and Anderson[12] convergence accelerators were also available.

Let us consider an SCF iterative procedure. Cycle n starts with the definition of a density matrix $\mathbf{D}_n(\mathbf{k})$, either obtained as an initial guess (at cycle 0) or from eigenvectors of the previous cycle. A Fock matrix $\mathbf{F}_n(\mathbf{k})$ is then obtained from this density matrix, and then diagonalized at each $\mathbf{k}$ point of the First Brillouin Zone to obtain the new eigenvectors $\mathbf{C}_n(\mathbf{k})$. These form the $\mathbf{D}_{n+1}(\mathbf{k})$ density matrix, and so on. In the DIIS procedure, at each iterative cycle n, instead of the Fock matrix $\mathbf{F}_n(\mathbf{k})$, an averaged effective Fock matrix is generated as a linear combination of the Fock matrices of previous iterations:

$$\overline{\mathbf{F}}_n = \sum_{i=1}^{n} c_i \mathbf{F}_i \ . \tag{A.1}$$

The c_i coefficients are obtained by minimizing a suitable error functional $\mathbf{e}$, subject to the constraint that $\sum_{i=1}^{n} c_i = 1$. This is obtained by solving the linear equation system:

$$\begin{pmatrix} \mathbf{e} & \mathbf{1}^T \\ \mathbf{1} & 0 \end{pmatrix} \begin{pmatrix} \mathbf{c} \\ \lambda \end{pmatrix} = \begin{pmatrix} \mathbf{0} \\ 1 \end{pmatrix} \ , \tag{A.2}$$

where $\mathbf{e}$ is an error matrix having the size of the iterative space up to cycle n and λ is a Lagrange multiplier. The error matrix is defined through scalar products of suitable error vectors in the Γ point ($\mathbf{k} = 0$) of the Brillouin zone:

$$e_{nm} = < \mathbf{e}_n(\Gamma) | \mathbf{e}_m(\Gamma) > \ . \tag{A.3}$$

Other choices are possible (such as considering all $\mathbf{k}$ points, either with equal weight or weighted by Kerker factors[13] to avoid charge sloshing) but the above has been identified as the best default choice since it works well in most cases and minimizes the amount of information to be stored on disk.[14] According to Pulay's commutator-DIIS (CDIIS) formulation,[10] we define the error vector for the SCF procedure as:

$$\mathbf{e}_n(\mathbf{k}) = \mathbf{F}_n(\mathbf{k})\mathbf{D}_n(\mathbf{k})\mathbf{S}(\mathbf{k}) - \mathbf{S}(\mathbf{k})\mathbf{D}_n(\mathbf{k})\mathbf{F}_n(\mathbf{k}) \ , \tag{A.4}$$

where $\mathbf{S}(\mathbf{k})$ is the overlap matrix. In the case of periodic systems, the CDIIS formulation is particularly convenient, with respect to Eq. (A.5) below, since it allows the number of occupied orbitals in a given $\mathbf{k}$ point to change from one iteration to another. Hence, in the case the system is conducting, or is an insulator that passes through a conducting state during the SCF iteration, it allows the "sloshing" of electronic charge through the Brillouin zone. Eq. (A.4) is the one implemented in CRYSTAL17 for the SCF procedure.

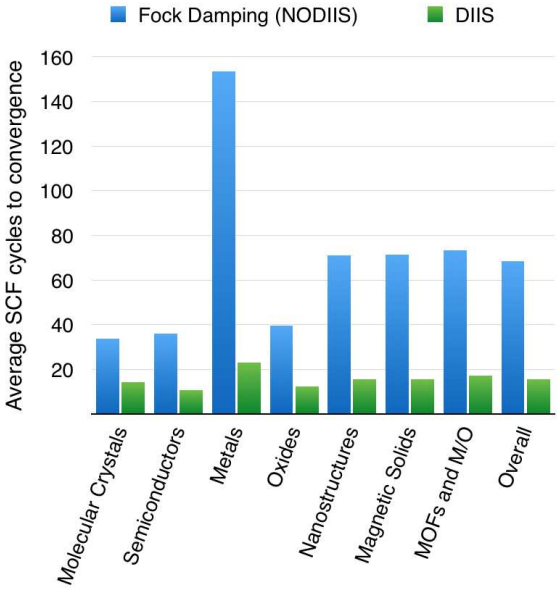

FIG. 2: Average SCF cycles needed to reach convergence with (green bars) and without (blue bars) DIIS convergence accelerator, as benchmarked on a test set of 42 periodic systems, grouped in 7 categories. MOF stands for Metal-Organic Frameworks and M/O for Metal/Oxide Interfaces. The rightmost column reports the global average. For more details see text.

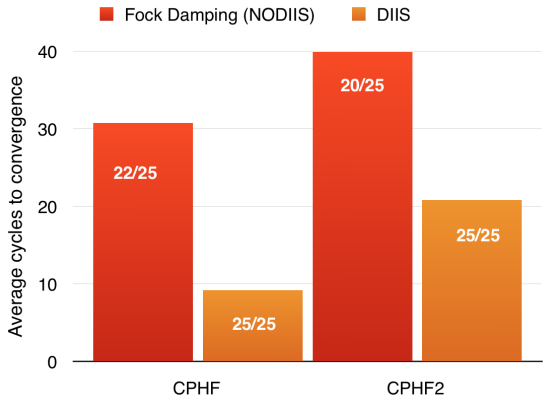

FIG. 3: Average CPHF and CPHF2 cycles needed to reach convergence with (red bars) and without (orange bars) DIIS convergence accelerator, as benchmarked on a test set of 25 periodic systems. White numbers reported on the bars indicate the number of calculations which reached convergence over the total of 25.

In Figure 2 we report the effect of the DIIS accelerator as compared with the Fock mixing + level shifting scheme that was default in CRYSTAL14, benchmarked on a representative test set of 42 periodic systems. The test set is described in detail in Ref. 14 and comprises 3D, 2D and 1D periodic systems, with basis sets ranging from minimal to quadruple-zeta. The 42 systems are equally divided in 7 groups according to their physico-chemical properties (molecular crystals, semiconductors, metals, oxides, nanostructures, magnetic solids, metal-organic frameworks and metal-oxide interfaces). Within each group Hartreee-Fock and 5 different functionals (LDA, PBE, PBE0, B3LYP, HSE06) were adopted. In all cases DIIS and NODIIS converged to the same solution, even though Fock mixing percentage had to be raised from 30% to 60% or even 90% in order to obtain convergence for the NODIIS case, for some systems. The threshold for convergence on energy was set in all cases to 10^{-10} Hartree.

It is easily seen from the rightmost bars of Fig. 2 that more than a factor of 3 in the number of SCF cycles is gained on average. The gain is consistent throughout the test set (in fact, in all cases DIIS is faster), and it is definitely more pronounced in the case of metallic systems, nanostructures (which includes graphene and carbon nanotubes) and magnetic systems.

The Coupled-Perturbed Hartree-Fock/Kohn-Sham (CPHF/KS) iterative procedure for the response to an external electric field $\mathcal{E}$ is similar to the SCF one outlined above, except that a density matrix perturbed by a field along Cartesian direction t is obtained at each cycle, $\mathbf{D}_n^{\mathcal{E}_t}(\mathbf{k})$. A perturbed Fock matrix is built and used to improve the perturbation matrix, without any diagonalization. For obtaining the formulation of the CPHF-DIIS error vector, it is convenient to start from the most general definition of the error vector:

$$|\mathbf{e}_n(\mathbf{k})>= \left[\mathbf{G}_n(\mathbf{k})\right]^{OV} = \mathbf{C}_n^{\mathrm{O}\,\dagger}(\mathbf{k})\mathbf{F}_n(\mathbf{k})\mathbf{C}_n^{\mathrm{V}}(\mathbf{k})\ , \quad \text{(A.5)}$$

where O and V superscripts indicate occupied and virtual blocks, respectively. Eq. (A.5) is completely equivalent to Eq. (A.4) if the orbital occupation does not change during the iterations, and this is precisely the case of CPHF/KS iterations, which apply a perturbative treatment to the already converged SCF solution. On the other hand, Eq. (A.5) is formally simpler than (A.4) and then easier to differentiate.

Then, the error vectors for the first– and second–order coupled perturbed procedures are obtained as:

$$|\mathbf{e}_n^{(\mathcal{E}_u)}(\mathbf{k})> \ = \frac{\partial|\mathbf{e}_n(\mathbf{k})>}{\partial\mathcal{E}_u} \quad \text{(A.6)}$$

$$|\mathbf{e}_n^{(\mathcal{E}_u,\mathcal{E}_v)}(\mathbf{k})> \ = \frac{\partial|\mathbf{e}_n(\mathbf{k})>}{\partial\mathcal{E}_u\partial\mathcal{E}_v}\ . \quad \text{(A.7)}$$

The full derivation and operative expression of such error vectors is provided in Ref. 14. Once computed, $|\mathbf{e}_n^{(\mathcal{E}_u)}(\mathbf{k})>$ or $|\mathbf{e}_n^{(\mathcal{E}_u,\mathcal{E}_v)}(\mathbf{k})>$ can be plugged in Eq. (A.3) so to obtain the DIIS error matrix and solve the linear equation system (A.2), identically as in the case of SCF iterations. Also in the case of CPHF/KS it turns out that the Γ-point only formulation of the error vector is sufficient for optimal performance and much more efficient from the point of view of information storage.[14]

In Figure 3 we report the average number of CPHF and CPHF2 cycles needed to reach convergence, as benchmarked on a subset of 25 of the 42 systems of Figure

2. The restriction of the set was mainly dictated by the impossibility of applying CPHF to conducting systems, and by the fact that functional derivatives for the range-separated HSE06 functional are not yet implemented in the code. Threshold on polarizability and second hyperpolarizability values was set to 10^{-4} a.u. Figure 3 shows that, roughly speaking, a factor of 3 is gained in CPHF, and of 2 in CPHF2. Most importantly, the DIIS procedure guaranteed convergence in all cases, which was not possible adopting the Fock damping scheme, not even with very high values of the damping percentage.

B. Thermal Properties through the Quasi-harmonic Approximation

Thermodynamic properties of solids can be computed with standard quantum-mechanical techniques by solving the lattice dynamics of the system and by applying the laws of statistical thermodynamics, through the definition of a canonical partition function. In a solid state context, the harmonic approximation (HA) to the lattice potential is usually adopted in the description of nuclear vibrations, which, as long as very light atoms (such as H, He, Li) are not present, provides a rather satisfactory description of most spectroscopic features of infrared, Raman and neutron-scattering spectra of materials.[15–27]

However, when it comes to thermodynamic properties, the limitations of the HA for solids are well-known. Indeed, the harmonic vibrational contribution to the internal energy of a crystal turns out to be independent of volume and thus many physical properties could not be properly described at this level of theory: i) thermal expansion would be null, ii) elastic constants would be independent of temperature, iii) constant-pressure and constant-volume thermodynamic properties (such as specific heat and entropy) would coincide with each other, iv) nuclear thermal conductivity would be infinite as well as phonon lifetimes, etc.[28,29]

In order to go beyond most of the above-mentioned limitations of the HA, the so-called quasi-harmonic approximation (QHA) can be invoked, which, due to its formal simplicity and relatively low computational cost, represents an effective method of choice for describing many anharmonic features of solids. The QHA essentially introduces the explicit volume dependence of phonon frequencies by retaining the simple harmonic expression for the Helmholtz free energy of the system (i.e. normal modes are still harmonic and independent of one another but now depend on volume):[30,31]

$$F^{\mathrm{QHA}}(T,V) = U_0^{\mathrm{ZP}}(V) + k_B T \sum_{\mathbf{k}p} \left[\ln\left(1 - e^{-\frac{\hbar\omega_{\mathbf{k}p}(V)}{k_B T}}\right)\right] , \tag{B.1}$$

where k_B is Boltzmann's constant and $U_0^{\mathrm{ZP}}(V)$ is the zero-temperature internal energy of the crystal which includes the zero-point energy of the system: $E_0^{\mathrm{ZP}}(V) = \sum_{\mathbf{k}p} \hbar\omega_{\mathbf{k}p}(V)/2$. The equilibrium volume $V(T)$ at a given temperature T is obtained by minimizing the isothermal Helmholtz free energy of Eq. (B.1) with respect to volume by keeping T as a fixed parameter. A volumetric thermal expansion coefficient $\alpha_V(T)$ can be defined as:

$$\alpha_V(T) = \frac{1}{V(T)} \left(\frac{\partial V(T)}{\partial T}\right)_{P=0} . \tag{B.2}$$

The temperature-dependent isothermal bulk modulus of the system, $K_T(T)$, can also be obtained as an isothermal second derivative of Eq. (B.1) with respect to the volume:

$$K_T(T) = V(T) \left(\frac{\partial^2 F^{\mathrm{QHA}}(V;T)}{\partial V^2}\right)_T . \tag{B.3}$$

The adiabatic bulk modulus $K_S(T)$ can also be evaluated within the QHA.[32] From the knowledge of $V(T)$, $\alpha(T)$ and $K_T(T)$, the difference between constant-pressure and constant-volume specific heats can also be computed at each temperature as:[33]

$$C_P(T) - C_V(T) = \alpha_V^2(T) K(T) V(T) T . \tag{B.4}$$

The QHA also allows for combining pressure and temperature effects on structural, elastic and thermodynamic properties of materials. By differentiating Eq. (B.1) with respect to the volume and changing sign, the thermal pressure is obtained:

$$P(V;T) = -\frac{\partial F^{\mathrm{QHA}}(V;T)}{\partial V} , \tag{B.5}$$

which can be used to evaluate the equilibrium volume, bulk modulus and thermodynamic functions at simultaneous high pressures and temperatures. The anisotropic thermal expansion of crystals can also be determined, by optimizing the lattice parameters with respect to the purely internal energy E at different volumes. In principle, a more accurate description of the anisotropic thermal expansion would be achieved by optimizing with respect to the free energy F,[34,35] which, however, would require a much larger set of calculations to be performed and would seldom result in significant changes.

Temperature-dependent elastic constants could also be obtained within the QHA as second free energy density derivatives with respect to the strain: $C_{vu}^T(T) = 1/V(T)[\partial^2 F/(\partial\eta_v \partial\eta_u)]$, which, however, would require the costly calculation of phonons at several strained lattice configurations.[36] A simpler way to obtain those thermo-elastic quantities is represented by the so-called quasi-static approximation (QSA),[37,38] which, taking advantage of the $V(T)$ relation obtained through the QHA, consists in evaluating static internal-energy E derivatives at the volume corresponding to the desired temperature: $C_{vu}^T(T) \approx 1/V(T)[\partial^2 E/(\partial\eta_v \partial\eta_u)]$.

A fully-automated scheme for computing the above-mentioned quasi-harmonic properties of crystals has been implemented in the new version of the CRYSTAL program, which relies on computing and fitting harmonic

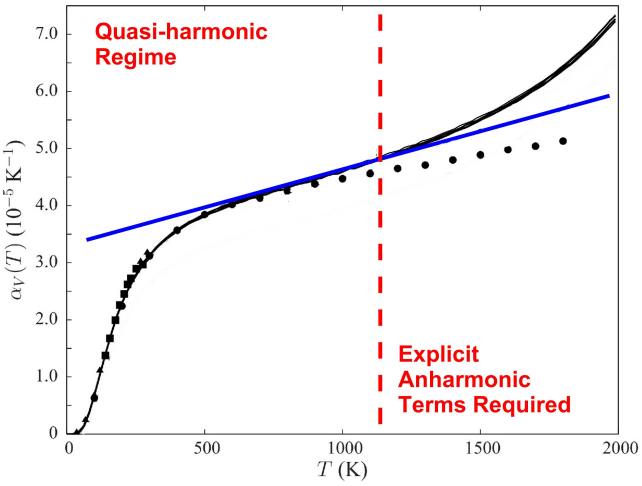

FIG. 4: Thermal expansion coefficient of MgO periclase as determined experimentally[42–44] (black symbols) and through quasi-harmonic lattice dynamical simulations[40] (black line). The QHA is expected to be valid only up to the temperature (marked by a vertical red dashed line) above which the computed thermal expansion coefficient starts deviating from linearity (the linear region is marked by a blue line).

vibration frequencies at different volumes (four volumes being enough for most systems) after having performed volume-constrained geometry optimizations.[32,39–41] The implemented algorithm requires a single calculation to be performed to get the whole set of thermal properties of the system.

It is worth stressing that the validity domain of the QHA (i.e. the temperature range in which it is expected to provide a reliable description of such thermodynamic properties) is strongly system-dependent and can hardly be expressed as a general function of the Debye temperature, θ_D, or melting temperature, T_M, of a material; it rather appears to be related to the chemical nature of the bond framework of the structure. In general, one might just expect that the weaker the interatomic interactions, the softer the phonon modes, the larger the intrinsic anharmonic effects and the smaller the validity domain.[45] If the validity domain of the QHA can not be predicted *a priori*, it can be determined *a posteriori*, according to the strategy sketched in Figure 4: i) the "high-temperature" linear behavior of the computed quasi-harmonic thermal expansion coefficient has to be identified (blue line in the figure); ii) the temperature above which the computed coefficient starts deviating from linearity (vertical red line in the figure) marks the upper-bound of the validity domain of the QHA. Above that temperature, an explicit treatment of the intrinsic anharmonicity of the potential (i.e. cubic and quartic terms mainly) would be required to get a reliable description of thermal features. It is worth mentioning that an external applied pressure tends to suppress down explicit anharmonic terms and thus to widen the applicability domain of the QHA with respect to the zero pressure case.[32,41]

The fully-automated implementation of the QHA in the CRYSTAL program has been applied to study several thermal properties (structural, elastic, thermodynamic, electronic) of various systems with different chemical features in the last couple of years: fully-covalent diamond,[39] ionic MgO and CaO,[40] LiF,[46] mixed ionic/covalent corundum α-Al_2O_3,[32] forsterite α-Mg_2SiO_4,[41] calcium stannate $CaSnO_3$,[47] and the molecular crystals of urea, purine and carbamazepine.[48–50] Some considerations can be done: i) in all cases, the evaluation of the vibration frequencies at just 4 volumes ensured stable and reliable results; ii) at variance with the determination of absolute values of constant-volume thermodynamic functions (which requires phonon dispersion to be carefully taken into account), the volume dependence of such thermodynamic quantities shows a fast convergence with respect to phonon dispersion sampling so that Γ-only vibration frequencies are enough for the latter in most systems; iii) again, at variance with their absolute values, the volumetric and thermal dependence of structural, elastic and thermodynamic properties of solids is found to be rather insensitive to the particular exchange-correlation functional used (with a slight systematic underestimation of the thermal expansion at the LDA level).

C. Dispersion-corrected Functionals and Composite Methods for Molecular Crystals

The proper description of noncovalent interactions requires the inclusion of long-range electron correlation effects that are missing in both HF and DFT methods. In particular, the treatment of the weak London forces is crucial because of their attractive and ubiquitous nature. They play a crucial role in many phenomena as for instance crystal packing of molecular solids, physisorption of molecules on surfaces or in microporous materials and interlayer interactions in layered materials.[51] A way to account for the missing dispersion energy in DFT is to augment the total energy as computed for a given density functional approximation with a dispersion term:[51,52]

$$E^{DFT-D} = E^{DFT} + E_{Disp} \; . \qquad \text{(C.1)}$$

An efficient and cost-effective approach is to use a simple atom-atom (e.g. 2-body) correction that includes the long-range dispersion energy through the asymptotic series (i.e. $-C_6/R^6 - C_8/R^8 - C_{10}/R^{10} - ...$) as:

$$E^{Disp} = -\sum_{AB} \sum_{n=6,8,10} \left(\frac{C_n^{AB}}{R_{AB}^n} \right) \; . \qquad \text{(C.2)}$$

In the new version of the code, the Grimme's DFT-D2 semiclassical dispersion correction[53,54] has been extended to the more recent DFT-D3 approach,[55] as implemented in a fully-automated way, which requires no definition of any input parameter by the user.

When using atom-centered basis sets, as in CRYSTAL, artificial dispersion mimicking effects can be present due to the basis set superposition error (BSSE) between interacting fragments. Indeed, BSSE gives a spurious extra-binding that mimics the dispersion energy and inconsistently sums to the dispersion correction. This becomes more relevant when small-to-medium size basis sets are employed and the system size increases. An empirical correction to BSSE for HF and DFT calculations has been recently proposed by Kruse and Grimme[56] that solely depends on the geometry of the system with the aim of reproducing the Boys-Bernardi counterpoise correction[57] through an atom-atom pairwise model. The method has been denoted as geometrical counterpoise correction (gCP). It can be applied in combination with the D2/D3 dispersion corrections to cancel out the BSSE and keep the correct asymptotic long-range decay of the dispersion energy.

By taking advantage of the combination of D3 and gCP corrections, an efficient composite approach HF-3c has been proposed by Sure and Grimme[58,59] that combines a minimal basis set HF calculation with three pairwise corrections: D3, gCP and an additional term to correct for short-range basis set incompleteness effects. In a similar fashion, another method, dubbed PBEh-3c, has been later proposed by Grimme and co-workers[59,60] aimed at making a step further in the trade-off of cost and accuracy with respect to HF-3c. Such a composite method is based on a revised version of the hybrid PBE0 functional that includes a larger amount of HF exchange (i.e 42%), the D3 (2- and 3-body terms) and gCP corrections in combination with a modified version of the def2-SVP basis set.[61]

The D3 and gCP corrections as well as both HF-3c and PBEh-3c approaches, originally proposed for molecular calculations, have been extended to periodic systems and implemented in the CRYSTAL17 code[62–65] The two composite methods are particularly targeted to model molecular crystals. For instance, in Table 1 a statistical analysis on the performance of these composite methods as compared to standard ones is reported. The analysis is performed on the optimized unit cell volume and on the corresponding lattice energy for the X23 dataset[66,67] of molecular crystals.

HF-3c gives good results in spite of its semiempirical nature. A slightly modified version in which the two-body C_8 term of the D3 correction is scaled by 0.27, improves significantly the agreement for predicted geometries. This modified HF-3c version can then be used either as a low-cost initial guess for a geometry optimization or as reference geometries for single-point energy calculation with higher level methods. For instance, the combination of B3LYP-D*/TZP//HF-3c (denoted as SP-B3LYP[65] in Table 1) gives cohesive energies of comparable accuracy as the full B3LYP-D*/TZP approach. The good accuracy of the HF-3c method makes it interesting for application to larger sets of molecular crystals. Indeed, in Ref. 65 it has been successfully applied to a set of 87 molecular crystals. From Table 1, it can also be seen that PBEh-3c performs equally well for both geometries and lattice energies with an accuracy comparable to the more costly B3LYP-D*/TZP method.

TABLE 1: Statistical indicators for the composite and reference methods for unit cell volumes V (in %) and lattice energies LE (in kJ/mol) of the X23 benchmark set (deviations from experimental reference values). Data are reported in the following format: Mean Absolute Error±Standard Deviation (Maximum absolute error).

Method	V (%)	LE (kJ/mol)	Ref.
HF-3c	8.0±2.5 (12.4)	8.2±8.8 (21.3)	65
HF-3c (0.27 s_8)	1.9 ± 2.3 (5.0)	13.1±8.7 (26.6)	65
PBEh-3c	2.7±3.2 (10.2)	5.4±7.1 (15.5)	60
B3LYP-D*/TZP	3.0±1.9 (6.0)	4.6±6.0 (17.9)	65
SP-B3LYP-D*		5.2±5.8 (15.6)	65

D. Strain-related Properties: Elasticity, Piezoelectricity, Piezo-optics

First-principle calculations based on the density functional theory (DFT) are known to represent an effective way to the accurate determination of many tensorial strain-related properties of solids: third-rank direct and converse piezoelectric, fourth-rank elastic stiffness and compliance, fourth-rank photo-elastic and piezo-optic tensors.[68–86] The quantum-mechanical determination of such high-order tensorial properties involves the evaluation of high-order total energy derivatives with respect to three main kinds of perturbations: periodicity-preserving atomic displacements, homogeneous strains and electric fields. If the main formal aspects related to the systematic treatment of these three perturbations, when combined together up to second- and third-order, have now been understood,[87,88] the determination of all components of any of these high-order tensors still represents a computationally demanding task from a practical perspective. This is due to the fact that a large number of fundamental calculations is required, which, in most implementations have to be performed independently *via* external programs or scripts.[80,89]

In the implementation of strain-related tensorial properties of solids into the CRYSTAL program, we have tried to devise fully-automated algorithms, capable of managing the large number of required calculations thus eliminating any intermediate action from the user, so that now each strain-related tensorial property mentioned above can be computed by running a single-calculation of the main program. An account of these developments has recently been reported.[90] In the following of this Section, we summarize the main developments made for these

properties in the CRYSTAL17 version of the program with respect to CRYSTAL14.

1. Elastic Constants Under Pressure

At zero pressure, second-order elastic constants are defined as second energy density derivatives with respect to pairs of infinitesimal Eulerian strains, as evaluated at the equilibrium volume V_0:

$$C^0_{ijkl} = \frac{1}{V_0}\left(\frac{\partial^2 E}{\partial\eta_{ij}\partial\eta_{kl}}\right)_{\eta=0}, \qquad \text{(D.1)}$$

where $\boldsymbol{\eta}$ is the second-rank symmetric pure strain tensor and i,j,k,l are Cartesian indices. A fully-automated scheme (with a full exploitation of point-symmetry) for the calculation of the whole elastic tensor was implemented in previous versions of the CRYSTAL program,[77,78] also for low-dimensionality, 1D and 2D, systems.[91]

When a finite pre-stress $\boldsymbol{\sigma}^{\rm pre}$ is applied in the form of a hydrostatic pressure P, within the frame of finite Eulerian strain, the elastic stiffness constants become:[33,76,92–94]

$$C_{ijkl} = C^0_{ijkl} + \frac{P}{2}(2\delta_{ij}\delta_{kl} - \delta_{il}\delta_{jk} - \delta_{ik}\delta_{jl}), \qquad \text{(D.2)}$$

where δ_{ij} are Kronecker's delta and provided that V_0 in equation (D.1) is replaced by the equilibrium volume $V(P)$ at pressure P. An implementation in the CRYSTAL17 program of the calculation of the stiffness tensor $\mathbb{C}$ (and of related elastic properties) under pressure has recently been presented[95] and applied,[96–98] which relies on the evaluation of the analytical stress tensor.[99–101] Let us introduce a two-index representation of the elastic stiffness tensor to be used below ($C_{ijkl} \rightarrow C_{vu}$), by exploiting Voigt's notation, according to which $v, u = 1, \ldots, 6$ ($1 = xx$, $2 = yy$, $3 = zz$, $4 = yz$, $5 = xz$, $6 = xy$).[102]

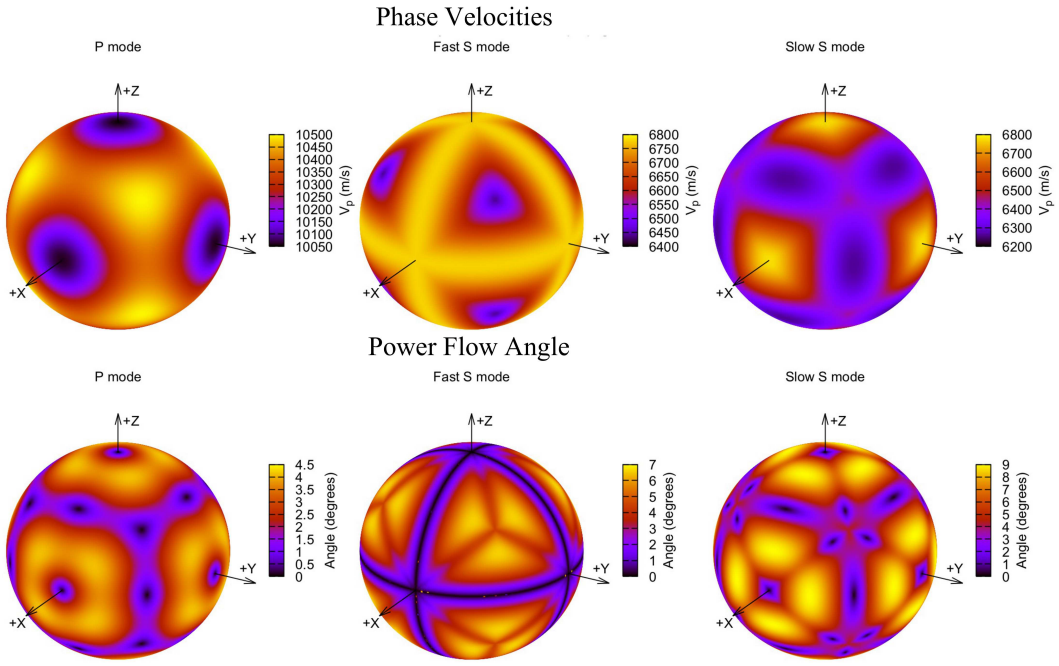

FIG. 5: Upper panels: elastic wave phase velocities as a function of propagation direction; lower panels: the corresponding power flow angles as a function of propagation direction. Data refer to the simple cubic crystal of MgO.

2. Elastic Wave Velocities

Once the fourth-rank elastic stiffness tensor of Eq. (D.1) has been computed, directional elastic wave velocities can be determined. Indeed, according to the elastic continuum theory, the velocities of the acoustic waves propagating along a direction represented by the unit wave-vector $\hat{\mathbf{q}}$ are obtained by solving Christoffel's equation, which can be given an eigenvalues/eigenvectors

form as follows:[103,104]

$$\mathbf{A}^{\hat{\mathbf{q}}}\mathbf{U} = \mathbf{V}^2\mathbf{U} \qquad \text{with} \qquad A^{\hat{\mathbf{q}}}_{kl} = \frac{1}{\rho}\sum_{ij}\hat{q}_i C_{iklj}\hat{q}_j \ , \tag{D.3}$$

where ρ is the crystal density, $\hat{q}_i$ is the i-th element of the unit vector $\hat{\mathbf{q}}$, $\mathbf{V}$ is a 3×3 diagonal matrix whose three elements give the acoustic phase velocities and $\mathbf{U}$ = ($\hat{\mathbf{u}}_1$,$\hat{\mathbf{u}}_2$,$\hat{\mathbf{u}}_3$) is the eigenvectors 3×3 matrix where each column represents the polarization $\hat{\mathbf{u}}$ of the corresponding eigenvalue. The three acoustic wave velocities can be labeled as quasi-longitudinal v_p (P mode), slow quasi-transverse v_{s1} (slow S mode) and fast quasi-transverse v_{s2} (fast S mode), depending on the polarization direction $\hat{\mathbf{u}}$ with respect to wave-vector $\hat{\mathbf{q}}$.[76]

In CRYSTAL17, phase and group elastic wave velocities, as well as the related power flow angles and enhancement factors, can be computed for all crystallographic directions in the same calculation of the elastic tensor *via* the AWESOME code by Muñoz-Santiburcio *et al.*, which has been merged and has become a keyword of CRYSTAL17.[105,106] This option allows to represent the computed properties according to different graphical representations. An example, referring to the simple MgO cubic crystal, is given in Figure 5, where the three elastic wave phase velocities (for the P mode, slow S mode and fast S mode) and the corresponding power flow angles (i.e. the angles ψ linking phase V_p and group V_g velocities through $V_g = V_p/cos(\psi)$) are represented in polar plots, as a function of propagation direction. We refer to Ref. 105 for the definition of all quantities.

3. Analytical Direct Piezoelectricity

The direct proper piezoelectricity of a non-centrosymmetric crystal is usually evaluated numerically through the Berry-phase approach.[68–70] This was also the case in previous versions of the CRYSTAL program.[107,108] In particular, in the CRYSTAL14 version, a fully-automated algorithm was implemented for computing the direct piezoelectric tensor via the Berry-phase approach,[71] which was also generalized to low-dimensional 1D and 2D systems.[91] In these implementations, the nuclear relaxation term was accounted for by performing geometry optimizations of atomic positions at strained lattice configurations.

In CRYSTAL17, a fully-automated scheme has now been implemented for the quasi-analytical calculation of the direct piezoelectric tensor where the electric dipole derivatives in both the electronic "clamped nuclei" and "nuclear relaxation" terms are computed through the CPHF/KS approach.[109] In addition, the "nuclear relaxation" term is evaluated using the "internal-strain" tensor as combined with the interatomic force constant matrix (see Section II D 4 for more details).[110] With this new strategy, the original shape of the lattice cell is preserved at all steps of the calculation.

4. The Internal-strain Tensor

Strain-induced response properties of solids can be formally decomposed into a purely electronic "clamped-nuclei" term and a nuclear-relaxation term due to the rearrangement of atomic positions upon strain. The evaluation of the latter is generally much more computationally expensive than that of the former. In principle, two alternative approaches can be used to account for nuclear-relaxation effects: i) performing numerical geometry optimizations to relax atomic positions at actual strained lattice configurations,[111,112] or ii) evaluating in a more analytical fashion the "internal-strain" tensor of energy second-derivatives with respect to atomic displacements and lattice deformations, as combined with the interatomic force constant Hessian matrix.[87] Given that geometry optimizations at strained configurations are rather slowly-converging numerical procedures requiring particularly tight convergence criteria, the second approach is to be preferred as it ensures higher accuracy and requires less severe computational parameters to be used.[113]

As a matter of fact, in previous versions of the CRYSTAL program, only the first numerical strategy was available. In CRYSTAL17, the second approach has now been implemented for the elastic and piezoelectric tensors, which relies on the calculation of the "internal-strain" tensor by fully-exploiting its point-symmetry features.[110] Beside being more robust, the new strategy has also been documented to be more computationally efficient for most crystalline systems.[90]

The elements of the force-response internal-strain tensor are second-energy derivatives with respect to an atomic displacement and to a lattice distortion:

$$\Lambda_{ai,v} = \left.\frac{\partial^2 E}{\partial u_{ai}\partial\eta_v}\right|_{\mathcal{E}} , \tag{D.4}$$

where u_{ai} are Cartesian components of the displacement vector $\mathbf{u}_a$ of atom a (i=x,y,z). A displacement-response internal-strain tensor $\mathbf{\Gamma}$, which describes first-order atomic displacements as induced by a first-order strain, can be defined as:[87]

$$\Gamma_{ai,v} = -\left.\frac{\partial u_{ai}}{\partial\eta_v}\right|_{\mathcal{E}} = \sum_{bj}(H^{-1})_{ai,bj}\Lambda_{bj,v} \ , \tag{D.5}$$

where $\mathbf{H}$ is the interatomic force-constant Hessian matrix of energy second derivatives with respect to pairs of periodicity-preserving atomic displacements:

$$H_{ai,bj} = \left.\frac{\partial^2 E}{\partial u_{ai}\partial u_{bj}}\right|_{\mathcal{E},\eta} . \tag{D.6}$$

When mass-weighted and diagonalized, the force-constant matrix of Eq. (D.6) provides vibration frequencies of Brillouin zone-center phonon modes. The $\mathbf{H}^{-1}$

matrix in Eq. (D.5) has to be considered a pseudoinverse of $\mathbf{H}$ where translational degrees of freedom are projected out, as discussed in detail elsewhere.[87]

The nuclear-relaxation contribution to elastic and piezoelectric constants can be expressed in terms of the internal-strain tensor $\mathbf{\Lambda}$ (or $\mathbf{\Gamma}$):[87]

$$C_{vw}^{\rm nuc} = -\frac{1}{V_0}\sum_{ai}\Lambda_{ai,v}\Gamma_{ai,w}\ , \qquad \text{(D.7)}$$

$$e_{kv}^{\rm nuc} = -\frac{1}{V_0}\sum_{ai}Z^*_{k,ai}\Gamma_{ai,v}\ , \qquad \text{(D.8)}$$

where the $\mathbf{Z}^*$ tensor in Eq. (D.8) contains the Born dynamical effective charges:

$$Z^*_{k,ai} = \left.\frac{\partial^2 E}{\partial\mathcal{E}_k\partial u_{ai}}\right|_\eta\ . \qquad \text{(D.9)}$$

In the current fully-automated implementation into the CRYSTAL program, the elements $\Lambda_{ai,v}$ of the force-response internal-strain tensor are computed as finite differences of analytical lattice gradients with respect to atomic Cartesian displacements, by means of a generalized "Pulay's force method" originally proposed for interatomic force constants.[114] This strategy is quite computationally convenient as it requires the same atomic displacements to be considered as per the calculation of $\mathbf{H}$. As a consequence, $\mathbf{\Lambda}$ and $\mathbf{H}$ are computed simultaneously, nearly at the same computational cost as for the calculation of $\mathbf{H}$ alone.

5. *The Piezo-optic Tensor*

The anisotropy of the linear optical properties of a crystal can be represented by its *optical indicatrix*: an ellipsoid oriented along the principal axes of the dielectric tensor $\boldsymbol{\epsilon}$ and whose semi-axes give the principal refractive indices of the system.[102] Any change in the shape, size and orientation of the indicatrix would result in the modification/modulation of the linear optical properties of a material. Such changes can be induced by electric fields, strains and stresses giving rise to the electro-optic, elasto-optic and piezo-optic effects, respectively.

In the CRYSTAL14 version of the program a fully-automated algorithm was developed to compute the fourth-rank elasto-optic (or photo-elastic) tensor,[84] whose components p_{ijkl} measure the variation of the inverse dielectric tensor $\boldsymbol{\epsilon}^{-1}$ as induced by strain:

$$\Delta\epsilon^{-1}_{ij} = p_{ijkl}\eta_{kl}\ . \qquad \text{(D.10)}$$

As both the inverse dielectric tensor $\boldsymbol{\epsilon}^{-1}$ and the pure strain tensor $\boldsymbol{\eta}$ are symmetric, Voigt's notation can be adopted also in this case so that the photo-elastic tensor $\mathbf{p}$ can be given a 6×6 matrix representation as for the elastic tensor.

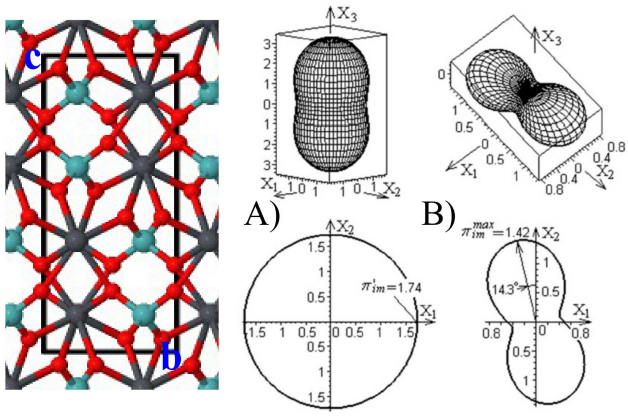

FIG. 6: Left panel: the crystal structure of tetragonal $PbMoO_4$. Right panel: indicative surfaces of the piezo-optic effect (in Brewster) of $PbMoO_4$ when a uniaxial pressure is applied parallel to the X_3 principal optical axis (A) and parallel to the X_1 principal optical axis (B).[86]

Given the stress-strain relation, the fourth-rank piezo-optic tensor $\boldsymbol{\pi}$ (whose elements are the stress-optical coefficients π_{vu}) can be obtained from the photo-elastic tensor $\mathbf{p}$ and elastic tensor $\mathbb{C}$ as:

$$\boldsymbol{\pi} = \mathbf{p}\,\mathbb{S} \qquad \text{and conversely} \qquad \mathbf{p} = \boldsymbol{\pi}\,\mathbb{C}\ . \qquad \text{(D.11)}$$

At variance with the elastic $\mathbb{C}$ and compliance $\mathbb{S}\equiv\mathbb{C}^{-1}$ tensors, $\mathbf{p}$ and $\boldsymbol{\pi}$ are not symmetric (*i.e.* in general $p_{vu}\neq p_{uv}$ and $\pi_{vu}\neq\pi_{uv}$). It follows that the number of symmetry-independent components to be determined for the stress-optical and strain-optical tensors is generally larger than for the elastic tensors.

In CRYSTAL17, a fully-automated algorithm has been developed to compute the whole fourth-rank piezo-optic tensor with a single-run calculation.[85] The piezo-optic effect has proven to be an effective tool for mapping 2D and 3D mechanical stresses through stress tensor-field tomography,[115,116] and is important in the field of opto-electronics where the search for highly efficient electro-optic and piezo-optic materials is experiencing a great interest in recent years due to their applications as photo-elastic modulators of light polarization and as components of many devices related to acousto-optic light modulators, deflectors, tunable spectral filters, etc.[104,117–123]

This scheme has recently been applied to the investigation of the piezo-optic response of tetragonal $CaWO_4$ and $PbMoO_4$, and monoclinic triglycine sulfate (TGS).[85,86,124] The anisotropy of the piezo-optic effect can be represented in terms of indicative surfaces. In Figure 6, two indicative surfaces are reported for the $PbMoO_4$ tetragonal crystal corresponding to two cases in which a uniaxial pressure is applied parallel to the X_3 and X_1 optical axes.

E. Dynamic Polarizabilities and First-hyperpolarizabilities: Second Harmonic Generation and Pockels Effects

The Coupled-Perturbed-Hartree-Fock/Kohn-Sham (CPHF/KS) scheme for dynamic (hyper)polarizabilities,[125] as adapted to periodic systems,[126] is a perturbative, self-consistent method that focuses on the description of the relaxation of the crystalline orbitals under the effect of an external frequency-dependent electric field. Starting from an unperturbed SCF solution at convergence, the electric field is introduced by means of standard perturbation theory and resulting equations are solved iteratively.

The adaptation to the periodic case is non-trivial, since the molecular form of the electric field operator ($\mathcal{E}\cdot\mathbf{r}$) is not bound and breaks translational invariance. Hence, a more complex expression formula has to be adopted[127–129] ($\mathcal{E}\cdot\imath e^{\imath\mathbf{k}\cdot\mathbf{r}}\boldsymbol{\nabla}_k e^{-\imath\mathbf{k}\cdot\mathbf{r}}$). The CPHF/KS method was first implemented in CRYSTAL09 for static fields, allowing for the calculation of the electronic contribution to the static polarizability tensor α (or ϵ^∞ dielectric tensor) of closed- and open-shell periodic systems.[130,131] The CPHF/KS scheme was further extended to second-order in the perturbed wavefunction in CRYSTAL14, thus allowing for the calculation of static nonlinear properties (namely, second hyperpolarizabilities and $n+1$ rule first hyperpolarizabilities).[132,133] The CPHF/KS approach is also used in the evaluation of observables that are obtained as a mixed derivative of the total energy, such as infrared and Raman intensities[20–22,134] and piezoelectric tensor.[109]

It is of great interest to go beyond the static limit, and study the interaction of crystalline solids with dynamic fields. In CRYSTAL17, the ω-frequency of the field has been introduced in the CPHF(KS) method. This allows the study of the variation of the real part of $\epsilon^\infty(\omega)$ and refractive index $n=\sqrt{\epsilon^\infty}$, with respect to the light wavelength.[135]

If the field is frequency-dependent, the determination of the dynamic polarizability for a closed-shell system is obtained as follows:

$$\alpha_{uv}(-\omega;+\omega) = -\frac{\partial^2 E^{TOT}}{\partial\mathcal{E}_{u[-\omega]}\partial\mathcal{E}_{v[\omega]}} = -\frac{2}{n_k}\Re\Big\{ P_{u[-\omega],v[+\omega]} \sum_{\mathbf{k}}^{BZ}\mathrm{Tr}\left[n\left(\boldsymbol{\Omega}^{(\mathcal{E}_{u[-\omega]})}(\mathbf{k})\mathbf{U}^{(\mathcal{E}_{\mathbf{v}[+\omega]})}(\mathbf{k})\right)\right]\Big\}\ , \quad \text{(E.1)}$$

where Tr signifies the trace, n_k is the number of k-points sampling the Brillouin zone (BZ), and P is a permutation operator.[136,137] $\boldsymbol{\Omega}^{(\mathcal{E}_u)}(\mathbf{k})$ corresponds to the matrix of the operator $\hat{\Omega}^{(\mathcal{E}_u)} = u + i\nabla_{k_u}$ in the AO basis, t,u,v are Cartesian directions, n is the diagonal occupation matrix, with eigenvalues either equal to 2 (for occupied orbitals, in a closed-shell case) or equal to 0 (for virtual orbitals). The $\mathbf{U}$ matrices, that determine the first-order perturbed orbitals, are obtained as:[135,138–140]

$$U_{ia}^{(\mathcal{E}_{t[\pm\omega]})}(\mathbf{k}) = \lim_{\eta\to 0^+}\frac{G_{ia}^{(\mathcal{E}_{t[\pm\omega]})}(\mathbf{k})}{\epsilon_a^{(0)}(\mathbf{k})-\epsilon_i^{(0)}(\mathbf{k})\pm\omega+\imath\eta}\ , \quad \text{(E.2)}$$

where $G_{ia}^{(\mathcal{E}_{t[\pm\omega]})}(\mathbf{k})$ is the derivative of the Fock matrix element with respect to the ω-frequency dependent field along t-direction, which has subsequently been projected onto the unperturbed crystalline orbital basis set:

$$G_{ia}^{(\mathcal{E}_t[\pm\omega])}(\mathbf{k}) = \sum_{\mu,\nu} C^*_{\mu i}(\mathbf{k}) F_{\mu,\nu}^{(\mathcal{E}_t[\pm\omega])}(\mathbf{k}) C_{\nu a}(\mathbf{k}) \quad , \quad \text{(E.3)}$$

and $\epsilon_{i(a)}^{(0)}(\mathbf{k})$ is the unperturbed eigenvalue of the occupied i (virtual a) crystalline orbital for each k-point ($\mathbf{k}$) of the reciprocal space. Since $\boldsymbol{F}^{(\mathcal{E}_t[\pm\omega])}(\mathbf{k})$ and, thereby, $\boldsymbol{G}^{(\mathcal{E}_{t[\pm\omega]})}(\mathbf{k})$ depends upon $\boldsymbol{U}$ the solution of Eq. (E.2) for the $U^{(\mathcal{E}_t[\pm\omega])}(\mathbf{k})$ matrices is obtained by fixing the value of ω and then solving iteratively.

A formula for the dynamic first hyperpolarizability can be obtained starting with the $2n+1$ rule working expression for the static limit (see Eq. 58 in Ref. 141), which has the same form as that shown below except, of course, that all frequencies are set equal to zero. The 3D static result was obtained, in fact, by generalizing the 1D periodic frequency-dependent treatment of Kirtman *et al.*[142] which, in turn, was based on the time-dependent Hartree-Fock formulation for molecules developed by Karna and Dupuis.[139] The latter treatment has been generalized so as to be applicable for arbitrary frequencies and periodic systems. In addition, we introduce the operator $P_{t[-\omega_\sigma]u[+\omega_1]v[+\omega_2]}$ which permutes the pairs $(t[-\omega_\sigma])$, $(u[+\omega_1])$, and $(v[+\omega_2])$.[136,137] From the approach just described the general expression for the first hyperpolarizability of closed-shell periodic systems in the presence of frequency-dependent fields may be written as:[143]

$$\beta_{tuv}(-\omega_\sigma;\omega_1,\omega_2) = -\frac{\partial^3 E^{TOT}}{\partial\mathcal{E}_{t[-\omega_\sigma]}\partial\mathcal{E}_{u[\omega_1]}\partial\mathcal{E}_{v[\omega_2]}} = -\frac{2}{n_k}\Re\Big\{P_{t[-\omega_\sigma],u[+\omega_1],v[+\omega_2]} \sum_{\mathbf{k}}^{BZ}\mathrm{Tr}\left[n\,\mathbf{U}^{(\mathcal{E}_{t[-\omega\sigma]})\,\dagger}(\mathbf{k})\left(\mathbf{G}^{(\mathcal{E}_{\mathbf{u}[+\omega_1]})}(\mathbf{k})\mathbf{U}^{(\mathcal{E}_{\mathbf{v}[+\omega_2]})}(\mathbf{k}) - \mathbf{U}^{(\mathcal{E}_{\mathbf{v}[+\omega_2]})}(\mathbf{k})\mathbf{G}^{(\mathcal{E}_{\mathbf{u}[+\omega_1]})}(\mathbf{k}) + \imath\frac{\partial\mathbf{U}^{(\mathcal{E}_{\mathbf{v}[+\omega_2]})}(\mathbf{k})}{\partial\mathbf{k_u}}\right)\right]\Big\}\ . \quad \text{(E.4)}$$

The full derivation of Eq. (E.4) alongside with a robust validation of the implementation is reported in Ref. 144.

Such third-order rank tensor depends on the three Cartesian directions of the field t, u, v, and on three frequencies, ω_σ, ω_1 and ω_2 with $\omega_\sigma = \omega_1 + \omega_2$. The last term of Eq. (E.4) appears only for infinite periodic systems.

Eqs. (E.1) and (E.4) hold for Hartree-Fock. The extension to KS-DFT has also been carried out in the previous work (Ref. 145 for the static case, Ref. 144 for the dynamic) and implemented in the CRYSTAL code. We do not repeat the DFT expression here since it is quite long (e.g. see Eq. 8 of Ref. 144), even though straightforward to evaluate.

Among all possible choices of ω_1 an ω_2, there are two cases of particular relevance: i) Second Harmonic Generation (SHG), in which $\omega_1 = \omega_2 = \omega$ and $\omega_\sigma = 2\omega$, and ii) dc-Pockels effect, in which $\omega_1 = \omega$, $\omega_2 = 0$ and $\omega_\sigma = \omega$.

As a demonstrative application, we report in Figure 7 the SHG d_{xyz} component of the molecular crystal of urea as a function of the wavelength for different Hamiltonians.[143] The $\mathbf{d}$ tensor is directly obtained from $\boldsymbol{\beta}$ via the relation $\mathbf{d} = \frac{\pi}{V}\boldsymbol{\beta}$, with V being the unit cell volume. The other non-vanishing component, d_{zxy}, has a similar dispersion behavior and has not been plotted. We can see in the figure that the curves for the various methods remain practically parallel except as one approaches the first resonance. It clearly shows the well-known tendency of LDA and GGA functionals to largely overestimate high-order electric susceptibilities, which is exaggerated near the first resonance. It is noteworthy that d_{xyz} increases at each frequency when the percentage of HF-exchange decreases. This is not unexpected because it correlates with the predicted band gap for the different Hamiltonians which decreases from HF (14.0 eV) to PBE0 (7.4 eV) and B3LYP (6.9 eV) to PBE (5.2 eV) and LDA (4.8 eV).

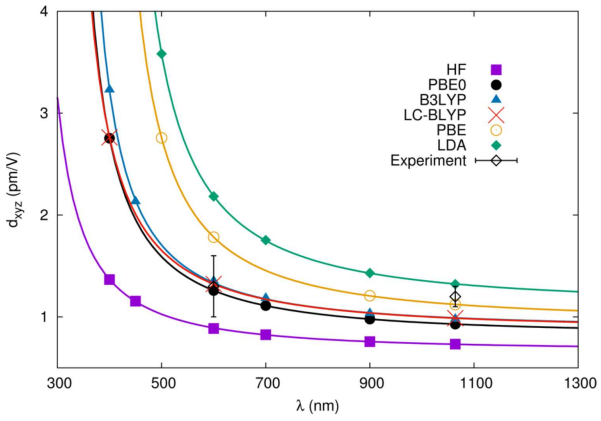

FIG. 7: SHG d_{xyz} tensor component of bulk urea as a function of wavelength $\lambda = 2\pi/\omega$, as obtained with various functionals. The computed data are fit to the three parameter function: $d(\lambda) = a + b(1/(\omega_0 - 2\omega)(\omega_0 - \omega) + 1/(\omega_0 + \omega)(\omega_0 - \omega) + 1/(\omega_0 + \omega)(\omega_0 + 2\omega))$.

F. Hybrid Functionals

Within the framework of the density-functional-theory (DFT), a class of functionals of particular interest is represented by so-called *hybrids*, which, by introducing a fraction of exact non-local Fock exchange, partially correct for the self-interaction error of local or semilocal formulations.[146]

In a molecular context, hybrid functionals have been widely used in the last couple of decades, since their original formulation by Becke in 1993.[147] Their advantages over local-density (LDA) and generalized-gradient (GGA) approximations are well-known and extensively documented in terms of an improved description of a large set of properties (from thermochemical formation energies to molecular structures, vibration frequencies, polarizabilities, chemical shifts, hyperfine coupling constants, and others).[146,148–153]

In a solid state context, the advantages of the hybrid approach grow to an even greater extent because of their better description of mechanical, dielectric, optical properties (leading to more reliable values for the electronic band gap, for instance), and of electron localization, which is crucial to the study of magnetic properties, defects, transition-metal compounds, spin-polarized systems, etc.[154–157] Despite these clear advantages, their popularity for material modeling has been significantly hindered for many years by the high computational cost of their plane-wave implementations, particularly so for the original full-range (i.e. global) formulation compared to recent screened-exchange ones.[158–161]

By use of a basis set of atom-centered localized Gaussian-type functions instead of plane waves, Fock exchange was demonstrated to be very efficiently computable for any range.[162] This satisfied a fundamental prerequisite for the first implementation of a Hartree-Fock (HF) code for solids: CRYSTAL, first released in 1988.[5] Within such a local basis set formalism, a mixed DFT/HF approach for solids was already implemented in 1987 based on an *a posteriori* correlation correction to the Hartree-Fock total energy of periodic systems using the Colle-Salvetti density functional.[163,164] *A priori* hybrid functionals were first included for solids in the CRYSTAL95 version of the program (only a couple of years later than Becke's original proposal) and have been available to the community of solid state physicists and chemists since then.[165]

1. *Self-Consistent Hybrids*

For a long time, hybrid functionals (either global or screened-exchange) have been characterized by a fixed, system-independent Fock exchange fraction α (0.2 in B3LYP, 0.25 in PBE0 and HSE06, 0.16 in B1WC, for instance).[147,166–168] Many properties of solids turn out to be significantly affected by the α parameter, which makes the identification of its optimal value important.

For instance, it is known that the electronic band structure of small or large band gap solids is better reproduced by use of smaller or larger values of α, respectively.[154,169]

In recent years, the use of a system-specific optimal exchange fraction, linked to the static electronic screening of the system, has been suggested. In this proposal, α is chosen to be inversely proportional to the static electronic dielectric constant ϵ_∞ of the material.[169–174] The dielectric constant in the functional is either taken from experiment or computed. Skone *et al.* have recently proposed a promising iterative scheme for the calculation of the optimal Fock exchange fraction of global hybrids, where the static electronic dielectric response of the material and α are self-consistently determined.[175] Self-consistent hybrids are becoming popular in solid state applications mainly because of their reliable description of the electronic band structure and some optical properties.[176–185]

The system-specific character of self-consistent hybrid functionals has the advantage of improving the electronic screening in the material but makes it necessary to determine α for each system as a pre-step to any calculation. This implies higher computational cost and reduced user-friendliness compared to standard hybrids, unless computationally-efficient, automated strategies are devised. A fully-automated (i.e. requiring a single calculation), computationally-efficient implementation of self-consistent hybrid functionals has been coded into the CRYSTAL17 program.[186] The static electronic dielectric tensor of the system is computed by adopting a Coupled-Perturbed-Hartree-Fock/Kohn-Sham (CPHF/KS) approach with full advantage taken of internal guesses for the perturbed and unperturbed density matrices from previous iterations to achieve high computational efficiency. The latter has been documented to reduce the computational cost of the whole process by at least a factor of 2.

2. Range-Separated Hybrids

Range-separated (RS) hybrid functionals have received more and more attention in the last years for application in quantum chemistry calculations. Unlike global hybrid functionals, in RS hybrids the constant amount of HF exchange is usually replaced by a contribution either at short-range (i.e. screened Coulomb range-separated hybrids, SC-RSH) or at long-range (i.e. long-range corrected hybrids, LC-RSH) as a function of a given range-separation parameter. In particular, the inclusion of HF exchange at long-range recovers the correct decay of the exchange potential and reduces the self-interaction error that plagues standard exchange-correlation functionals. It turns out that LC-RSH methods show better performance in the prediction of valence occupied and unoccupied orbital energies, charge transfer excitation energies and in the evaluation of dielectric response properties such as first- and second-hyperpolarizabilities.[187]

In CRYSTAL17, a bunch of range-separated hybrid functionals (RSHXLDA,[188,189] ω-B97, ω-B97X,[190] LC-BLYP[191,192] and CAM-B3LYP[193]) has been extended to the CPHF/KS scheme thus allowing for the calculation of linear and nonlinear optical properties with these methods. An example of application of LC-RSH to the prediction of the SHG electric susceptibility of the urea crystal is shown in Figure 7. The results for the long-range corrected hybrid functional based on the Iirikura-Tsuneda-Yanai-Hirao scheme, LC-BLYP,[191,192] are in good agreement with experimental values.[143] The LC-BLYP functional has also been recently applied to the prediction of the dipole polarizabilities of hBN–graphene hybrid structures for finite (0D) and periodic (2D) models[194] and of infinite linear chains of phenalenyl radicals.[195]

G. Massively-Parallel Version for Large Systems

In order to extend the application domain of standard *ab initio* and DFT methods in a solid state context, the possibility of investigating larger, progressively more realistic, systems is obviously crucial. A thorough exploitation of the opportunities brought by parallel computing represents a primary means of doing so, particularly when combined with high-performance computing (HPC) resources. Indeed, a clever exploitation of parallel computing allows not only for i) a faster time-to-solution, but also for ii) a reduction of the required memory per core, which makes the investigation of larger systems possible.

A replicated-data parallel version of the program, PCRYSTAL using message-passing-interface (MPI) directives, has been available since 1996, in which a complete copy of all necessary data for the calculations is held by every process, but different processes are performing different independent parts of the calculation at a given instant.[196] The evaluation of one- and two-electron integrals is very efficiently parallelized within this scheme, as independent subsets of integrals may be assigned to different processes. For the SCF procedure, parallelism is mainly achieved by exploiting the factorization of many computational tasks in reciprocal space (such as the Fourier transform of the main matrices, Kohn-Sham matrix diagonalization, etc.), into essentially independent **k**-points. When spin-unrestricted formulations are used for open-shell systems, parallelism is also extended to α and β spins. From the CRYSTAL14 version of the program, this kind of parallelism has further been pushed to include point-symmetry factorization within each **k**-point based on the corresponding irreps.[197] All features of the program can be computed with the replicated-data strategy, including one-electron properties through the recently-developed parallel version of the PROPERTIES module.[198] This strategy is particularly effective for systems containing up to several tens of symmetry-irreducible atoms per cell (say < 100) and a standard or dense sampling of reciprocal space.

A distributed-data massively-parallel version of the program, MPPCRYSTAL, has been available since 2010. In MPPCRYSTAL all the largest arrays required by a calculation are partitioned and distributed among the processes so that each process stores in memory only a fraction of the total array on which it operates, and ScaLAPACK libraries are used for performing linear algebra tasks.[199,200] In particular, all objects that depend upon the square of the system size, including such entities as the Kohn-Sham matrix and its eigenvectors, are either distributed in this way or have been eliminated from the code. Further, all large objects in direct space (such as Fock and density matrices for each direct lattice cell) are stored in their most compact "irreducible" form and deallocated when not needed (during the reciprocal space operations, for instance), thus reducing the memory footprint of the program. We also note that this compact representation scales linearly with the system size, not quadratically. Owing to the distributed-data strategy, the larger the number of processes, the smaller the required memory per process as each process holds a smaller part of the distributed matrices. Thus the distributed-data parallel version represents the ideal tool to study very large systems (containing several hundreds or thousands of atoms per cell), with little or no point-symmetry, and a coarse reciprocal space sampling. At variance with the replicated-data version, not all algorithms have been extended to the distributed-data strategy yet. Available algorithms include the ordinary self-consistent-field procedure, analytical gradients, geometry optimization, vibration frequencies and infrared intensities (through a Berry-phase approach), as well as elastic and piezoelectric tensors. Work is constantly in progress to extend this strategy to other properties.

In recent years, the massively-parallel version of the program has been improved in three respects: i) the required memory per core has been further reduced by adopting a direct strategy (according to which some arrays are recomputed when needed instead of being stored on memory) for smaller matrices, which would eventually constitute a memory bottleneck; ii) the scalability of the wall-clock time needed to complete the calculation with respect to the number of cores used has been improved. This requires almost all tasks (including those taking very little time for small- or medium-sized systems) to be efficiently parallelized; iii) the scalability with respect to system size has also been improved by means of a complete restructuring of the routines for the selection of Coulomb and exchange two-electron integrals. For systems with no point-symmetry (i.e. belonging to the P1 space group, which is often the case for very large systems) this produced a significant reduction of the prefactor cost. Here we only briefly address point ii). For a more detailed account on the recent improvements of the massively parallel version of CRYSTAL, we refer to Ref. 201.

Figure 8 documents the so-called *strong scaling* of the MPPCRYSTAL program, that is the wall-clock time speedup as a function of the number of processors used for a system of fixed size. The upper and lower panels refer to systems with 4,632 and 13,896 atoms per cell, respectively. Both systems are supercells (8 and 24 times larger) of a primitive cell containing 579 atoms, which is a structural model of the MCM-41 compound (amorphous mesoporous silica, with no point-symmetry). MCM-41 has been used as a benchmark in previous documentations of the MPPCRYSTAL parallel efficiency.[4,200] The PBE functional was used in combination with a 6-31G* Pople basis set (corresponding to 7,756 atomic orbitals,

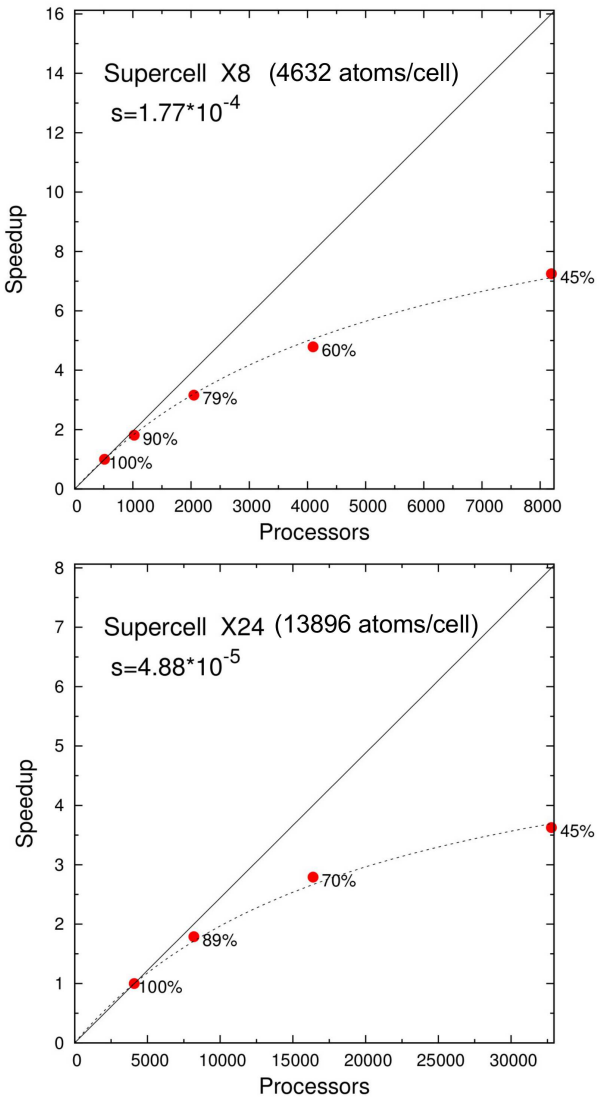

FIG. 8: Wall-clock time speedup of MPPCRYSTAL as a function of the number of cores used for the X8 (upper panel) and X24 (lower panel) supercells of the MCM-41 model (solution of the SCF procedure). The baseline used in the definition of the speedup is 512 and 4,096 cores for X8 and X24, respectively. The dashed line shows the fit of the speedup values to Amdahl's law. At each point, the scaling efficiency is reported (in %), where the diagonal of the plot corresponds to the ideal scaling.

AOs, per primitive cell). All calculations were run on the SuperMUC (LRZ, Germany) HPC IBM iDataPlex machine powered by 16 Intel cores per node running at 2.7 GHz, with 2 GB/core. A couple of key results:

- The largest calculation (system containing 13,896 atoms per cell) could be run in parallel over up to 32,768 processors;
- The wall-clock time speedup as a function of the number of processors shows a regular behavior and high scalability, due to the very high degree of parallelization of the entire code;

The last statement can be quantified by fitting the speedup values at different number of processors to the popular Amdahl model, which assumes that the code can be divided into a perfectly parallelized fraction p, and into a complementary sequential fraction $s = 1 - p$.[202] Dashed lines in Figure 8 represent the fitting to Amdahl's law. Despite the oversimplification introduced by this model, the measured speedup values are found to be nicely described by Amdahl's law. In each panel of the figure, the value of the fraction of the non-parallelized code s is reported, as determined from the fitting. Very low values of s are obtained, which document the high degree of parallelization of most (including irrelevant ones for smaller systems) steps in the calculation.

The parallel versions of the program have been extensively used in recent years to perform accurate quantum-mechanical simulations of structural, electronic, thermodynamic, spectroscopic, elastic and piezoelectric properties of a large variety of systems of different periodicity. Let us briefly review here those studies where the largest systems have been investigated so far (see Figure 9 for a graphical representation of the structure of some of them).

As regards non-periodic "molecular" systems, the structural, electronic and energetic properties of a family of (n,n) giant icosahedral carbon fullerenes have been investigated, for instance, where the largest system, corresponding to $n = 10$, contains 6,000 atoms. A basis set of 14 atomic orbitals per atom was used (84,000 AOs for the largest system) along with the global hybrid B3LYP functional.[203]

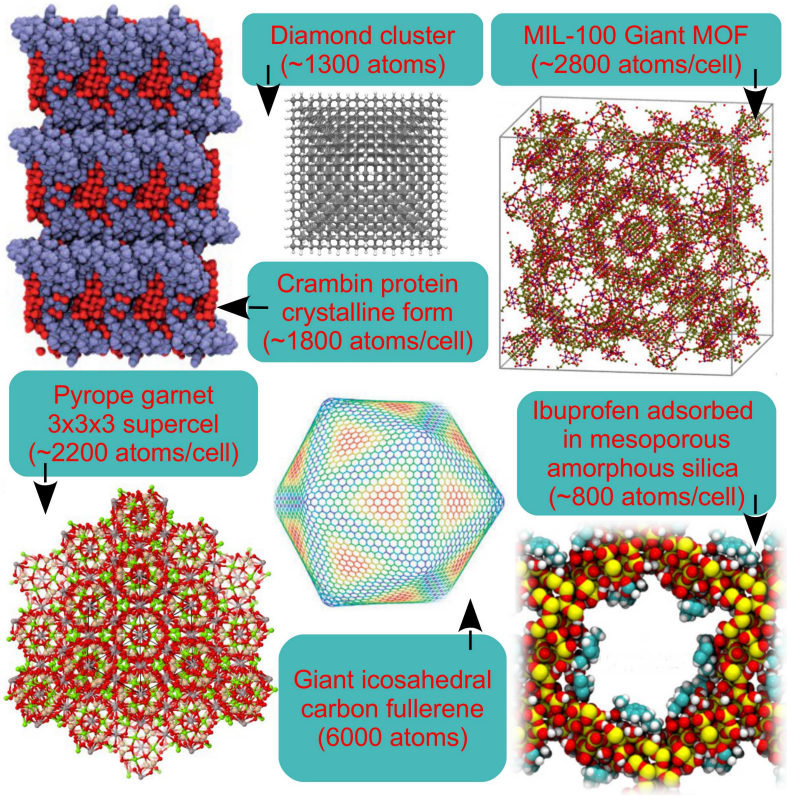

FIG. 9: Selected large-scale systems studied with the parallel versions of the CRYSTAL program in recent years. See text for the size of the basis set adopted for each system.

In another recent study, several features of non-periodic clusters, of increasing size (containing up to 1,293 atoms and about 13,000 AOs), of defective diamond were investigated at the hybrid B3LYP level and compared to the outcomes of fully periodic calculations.[204] Two different defects were put in the center of the clusters (a vacancy and the ⟨100⟩ split self-interstitial), whose structural, electronic and spectroscopic features were recently investigated with periodic calculations.[205,206] While structural and energetic features of the defects are found to be rather local and show a fast convergence with respect to the size of the model, other properties (such as the electronic band gap and the spectroscopic Raman fingerprint) are much more collective in nature and do show a very slow convergence.

As an example of a 1D periodic system, we refer to the recent investigation of structural and energetic properties of single-walled chrysotile [$Mg_3Si_2O_5(OH)_4$] nanotubes of increasing size, containing up to 5,004 atoms per unit cell, corresponding to about 90,000 AOs per cell and to a tube radius of 205 Å. Hybrid B3LYP calculations were performed and the stability of the rolled structures having the chirality $(n,-n)$ and (n,n), with respect to the flat slab of lizardite, was investigated. The appearance of clear minima in the energy profile as a function of the tube radius at about 89 Å was observed.[207]

More recently, one-dimensional stacked nanorings and nanohelices of elemental phosphorus were studied.[208] Structures up to 4,010 atoms and 108,270 AOs per unit cell – this is the case for the (20,1) helix – were studied in a few hours at the PBE0-D3 level with modest computational resources (12 CPU cores), thanks to the efficient exploitation of the 401 symmetry operators inherent to the system.

A cutting-edge study has recently been performed, by exploiting the capabilities of MPPCRYSTAL for the structural and energetic properties of the crystalline form of the "small" protein crambin. Crambin is a thionin hydrophobic protein with 46 amino acids and a distinct secondary structure characterized by both α-helices and β-sheets. The unit cell hosts two protein molecules (1,284 atoms). Two models of further structural complexity were considered by including an increasing number of solvating water molecules, up to 172, which brought the system to 1,800 atoms and 16,482 AOs per cell. Use of a global hybrid functional (B3LYP) was made in combination with a semi-empirical correction for dispersive interactions. The geometry was fully relaxed and found to agree to a large extent to that experimentally determined. The crystal formation, protein-water, and protein-protein interaction energies were computed.[209]

Large structural models (supercells of smaller unit cells, in this case) have to be considered also when the accurate determination of thermodynamic properties of solids is needed for the "direct-space" approach to phonon-dispersion. In a recent investigation, phonon dispersion and converged thermodynamic properties of two end-members of the silicate garnet family of rock-forming minerals (Pyrope $Mg_3Al_2Si_3O_{12}$ and Grossular $Ca_3Al_2Si_3O_{12}$) were determined with the hybrid B3LYP functional. The unit cell of these cubic systems contains 80 atoms; 3×3×3 super-cells were considered with 2,160 atoms and 40,176 AOs per cell (corresponding to sampling the phonon dispersion over 27 **k**-points within the Brillouin zone in reciprocal space). This allowed fully converged thermodynamic properties to be obtained as well as an understanding of the atomistic origin of the entropic difference between the two species.[27]

The capabilities of MPPCRYSTAL have also been exploited to shed some light on the atomistic details of the interaction between ibuprofen (one of the most common nonsteroidal anti-inflammatory drugs) and a realistic model of MCM-41 (one of the most studied mesoporous silica materials for drug delivery). Quantum-mechanical calculations (at the B3LYP-D level of theory) were performed to find the fully relaxed structure and to simulate the infrared spectrum.[210]

Structural, energetic and host/guest features of a giant metal-organic framework, MIL-100, containing up to 2,812 atoms per unit cell (and 50,256 AOs per cell) were also investigated. The interaction energy for CO_2 adsorption at different sites of the cavities was investigated.[211]

H. Tools for Magnetic Systems

The computationally efficient implementation of exact non-local Fock exchange makes the CRYSTAL program particularly suitable to study magnetic, spin-polarized, open-shell systems. Indeed, exact exchange is known to favor spin localization, which is crucial for a correct description of magnetic configurations both at short range (singlets, doublets, triplets, etc.) and at long range (ferromagnetism, anti-ferromagnetism, ferrimagnetism, etc.). In this section, we briefly review some of the improvements made in the program as regards open-shell systems.

1. Spin Contamination

When restricted spin-orbitals are used, the spatial orbitals are constrained to be identical for α and β spins ($\phi_i^\alpha = \phi_i^\beta$). On the contrary, unrestricted formulations work with spin-orbitals in which the spatial parts for α and β electrons can be different ($\phi_i^\alpha \neq \phi_i^\beta$). Although the removal of this constraint typically leads to lower energy solutions with respect to restricted cases, the unrestricted determinants are no longer guaranteed to be eigenfunctions of the $\hat{S}^2$ operator, as the wave-function is contaminated by terms with higher spin multiplicity.[212,213]

Let us consider an open-shell system with N_α spin-up electrons and $N_\beta < N_\alpha$ spin-down electrons. The spin contamination of an unrestricted solution is defined as follows (a molecular formalism is here adopted for sim-

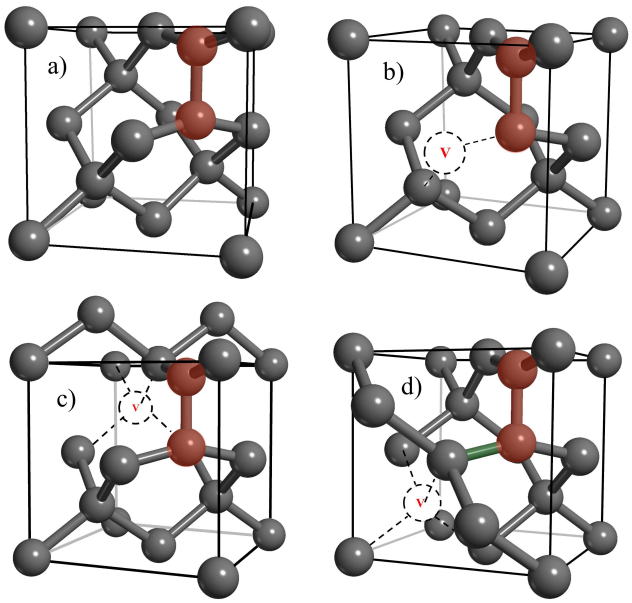

FIG. 10: Graphical representation of four point-defects in diamond: a) the ⟨100⟩ split self-interstitial (in red); b) the VI_1 defect where a vacancy and a self-interstitial are first neighbors; c) the VI_2^S defect where a vacancy is a second-neighbor of a self-interstitial with all C-C single bonds, and d) the VI_2^D defect where a vacancy is a second-neighbor of a self-interstitial with one C-C double bond (in green).

plicity):

$$\Delta S = \langle \hat{S}^2 \rangle - \langle \hat{S}^2 \rangle_{\text{pure}} = N_\beta - \sum_{i=1}^{N_\alpha} \sum_{j=1}^{N_\beta} \langle \phi_i^\alpha | \phi_j^\beta \rangle \langle \phi_j^\beta | \phi_i^\alpha \rangle \ , \tag{H.1}$$

where $\langle \hat{S}^2 \rangle_{\text{pure}}$ is the ideal expectation value of the $\hat{S}^2$ operator for a pure spin state:

$$\langle \hat{S}^2 \rangle_{\text{pure}} = S_z(S_z+1) \ \text{ with } \ S_z = \left(\frac{N_\alpha - N_\beta}{2} \right) . \tag{H.2}$$

In order to evaluate the spin contamination, the last term in Eq. (H.1) has to be computed, which can be rewritten as follows by expressing the spin-orbitals as a linear combination of atomic orbitals (AOs): $|\phi_i^\sigma\rangle = \sum_\mu C_\mu^{i\sigma} |\chi_\mu\rangle$, with σ either α or β:

$$\begin{aligned} \sum_{i=1}^{N_\alpha} \sum_{j=1}^{N_\beta} \langle \phi_i^\alpha | \phi_j^\beta \rangle \langle \phi_j^\beta | \phi_i^\alpha \rangle \ &= \\ \sum_{i,j}^{\text{occ.}} \sum_{\mu\nu\lambda\rho} C_\mu^{i_\alpha *} C_\nu^{j_\beta} C_\lambda^{j_\beta *} C_\rho^{i_\alpha} \langle \chi_\mu | \chi_\nu \rangle \langle \chi_\lambda | \chi_\rho \rangle \ &= \\ \sum_{\mu\nu\lambda\rho} P_{\rho\mu}^\alpha P_{\nu\lambda}^\beta S_{\mu\nu} S_{\lambda\rho} = \text{Tr}\left(\mathbf{P^\alpha S P^\beta S}\right) \ &, \end{aligned} \tag{H.3}$$

where $\mathbf{P}$ and $\mathbf{S}$ are the density and overlap matrices, respectively, in the basis of the AOs.

As an example, we consider several open shell electronic configurations of 4 different point defects of diamond: the ⟨100⟩ split self-interstitial defect (in both its singlet $S_z = 0$ and triplet $S_z = 1$ states), the VI_1 defect where a vacancy and a self-interstitial are first neighbors (in its singlet, triplet and quintuplet $S_z = 2$ states), the VI_2^S defect where a vacancy is a second-neighbor of a self-interstitial with all C-C single bonds, and the VI_2^D defect where a vacancy is a second-neighbor of a self-interstitial with one C-C double bond. A graphical representation of the structure of the four defects is given in Figure 10. The spin contamination ΔS, as introduced in Eq. (H.1), for the different systems and spin states is reported in Table 2, along with the total expectation value $\langle \hat{S}^2 \rangle$ and the ideal value of a pure state $\langle \hat{S}^2 \rangle_{\text{pure}}$. As one might expect, the spin contamination of high-spin electronic configurations (triplets and quintuplets) is always found to be rather small (i.e. it is never larger than 2.5%). On the contrary, low-spin states (i.e. singlets, with $S_z = 0$) are, in general, highly spin contaminated, which is an indication of the need for a multi-configurational treatment.

2. *Restricted Open Shell Hartree-Fock*

For the description of systems containing unpaired electrons, a single determinant might not be enough to accurately describe the spin features of the wave-function. In its general formulation,[214] the Restricted Open-shell Hartree-Fock (ROHF) wave-function is a sum of Slater determinants where each determinant contains a closed-shell subset (with doubly occupied orbitals) and an open-shell subset (with singly occupied orbitals). In the CRYSTAL code, the ROHF method was implemented in the early 90's for "half-closed shell" configurations, where the wave-function is still expressed as a single determinant.[215] Within this approach, two sets of orbitals are defined: in the first set orbitals are populated by paired electrons, in the second by unpaired electrons with parallel spin. This latter constraint allows the construction of wave-functions that are eigenstates of $\hat{S}^2$ but, on the other hand, does not allow for solutions with locally negative spin densities, which is mandatory for a correct description of anti-ferromagnetic systems, for instance.

Locally negative spin densities can be obtained within the Unrestricted Hartree-Fock (UHF) method, whose solutions are, however not pure eigenstates of $\hat{S}^2$. Due to its much larger variational flexibility, UHF has been preferred to ROHF. As a matter of fact, the ROHF implementation in the CRYSTAL program became obsolete a few years ago and was no longer available in the latest versions of the code. However, in recent years, there has been a renewed interest in ROHF solutions, mainly as an improved starting point for post-HF treatments,[216–222] which motivated us to restore the ROHF functionality in the program. A parallel implementation of ROHF has also been devised.

TABLE 2: The spin contamination ($\Delta S = \langle \hat{S}^2 \rangle - \langle \hat{S}^2 \rangle_{\rm pure}$) of different open-shell electronic configurations (characterized by different values of S_z) of four point-defects of diamond: the $\langle 100 \rangle$ split self-interstitial, and three different combinations of a vacancy with an interstitial.

System	S_z	$\langle \hat{S}^2 \rangle$	$\langle \hat{S}^2 \rangle_{\rm pure}$	ΔS
$\langle 100 \rangle$	0	1.0093	0.0000	1.0093
	1	2.0052	2.0000	0.0052
VI_1	0	0.0000	0.0000	0.0000
	1	2.0498	2.0000	0.0498
	2	6.0535	6.0000	0.0535
VI_2^S	0	1.4654	0.0000	1.4654
	1	2.0086	2.0000	0.0086
	2	6.0167	6.0000	0.0167
VI_2^D	0	1.6986	0.0000	1.6986
	2	6.0354	6.0000	0.0354

3. *Non-integer Spin Locking*

Convergence to an (anti)ferromagnetic ground state solution often requires locking the value of the desired total spin per cell, at least for the first few iterations of the SCF process. For metallic or half-metallic (anti)ferromagnets, it has now been made possible to fix the number of majority and minority spin electrons without forcing the calculation into an insulating state, also allowing for the calculation of unstable spin states in these systems. Furthermore, it is now possible to force the total spin to assume non-integer values, which often happens to be the case for the ground state in magnetic metals. This also allows to compute the static spin susceptibility $\chi_s = \partial M_s / \partial B$, where M_s is the spin magnetization and B the magnetic field, by finite differences using the formula $\chi_s = (\partial^2 E_{tot} / \partial {M_s}^2)^{-1}$.[223]

I. Hirshfeld-I Partitioning Scheme for the Electron Charge Density

Atomic charges represent one of the most popular concepts for the analysis of the electron density. However, the partition of the electron density into atomic contributions is not unique and thus several schemes have been proposed in this respect. In previous versions of the CRYSTAL program, Mulliken, Born and Bader charges could be computed. In CRYSTAL17, the Hirshfeld-I partitioning scheme (HI-I),[224] which presents some improvements with respect to the original Hirshfeld scheme,[225] has also been implemented.[226] In particular, an algorithm to deal with open-shell systems has been included, and the need to evaluate the promolecular density has been eliminated by implementing the Iterative Stockholder Atoms method.[227] The implementation full exploits the point-symmetry of the system and has been shown to scale linearly with the unit cell size.[226]

TABLE 3: Atomic charges (in $|e|$) of several crystals as calculated according to four different partitions of the electron density: a Mulliken's scheme, the Hirshfeld-I (HI-I) approach, Born charges, and Bader's QTAIM method. The time needed for running the corresponding calculations in parallel over 16 processors is also reported (in seconds).

System	Atom	Mulliken	HI-I	Born	QTAIM
LiF	Li	0.625	1.014	1.026	0.934
	F	-0.625	-1.014	-1.026	-0.934
	time (s)	1	18	13570	54148
BN	B	1.325	1.577	2.082	2.200
	N	-1.325	-1.577	-2.082	-2.200
	time (s)	0.1	114	5670	46084
α-Al_2O_3	Al	1.985	3.041	2.938	2.555
	O	-1.323	-2.027	-1.959	-1.703
	time (s)	0.1	119	21030	41225
Bayerite	Al	1.967	2.903	2.873	2.547
	O	-1.021	-1.547	-1.512	-1.456
	H	0.365	0.579	0.550	0.607
	time (s)	0.7	3784	156691	799965
Ice	O	-0.600	-0.898	-0.950	-1.246
	H	0.300	0.449	0.475	0.623
	time (s)	0.1	428	2714	44532

In Table 3, atomic charges as obtained with the HI-I method are reported and compared with Mulliken, Born (computed through an analytical CPHF/KS approach[228]), and Bader charges[229] from the Quantum Theory of Atoms in Molecules (QTAIM). The latter is considered to be one of the most rigorous (but costly) partitioning schemes. Several systems were considered covering a wide range of bonding types (ionic LiF, covalent hexagonal BN, mixed ionic/covalent corundum and bayerite, and the hydrogen-bonded ice molecular crystal). For sake of comparison, all the calculations were performed at the same B3LYP/TZP level by using the triple-zeta plus polarization basis set as optimized for solid-state calculations.[230] Since both the HI-I and Bader approaches require a dense numerical integration grid for the DFT part, the largest pre-defined grid was used; it corresponds to 99 radial and 1454 angular points. From the table, it is clearly seen that the Mulliken scheme systematically underestimates the atomic charges in comparison with all other methods. Apart from the case of covalent hexagonal BN, the HI-I approach provides atomic charges that are quite similar to the Born charges,

but at a significantly lower computational cost (by 1-2 orders of magnitude).

J. Vibrational Density-of-States and Inelastic Neutron Scattering Spectra

The calculation of harmonic vibration frequencies at the Γ point ($\mathbf{k} = \mathbf{0}$, the center of the First Brillouin Zone, FBZ) is available since the CRYSTAL03 version of the program and relies on the diagonalization of the mass-weighted Hessian matrix:

$$W^{\Gamma}_{ai,bj} = \frac{H^{\mathbf{0}}_{ai,bj}}{\sqrt{M_a M_b}} \quad \text{with} \quad H^{\mathbf{0}}_{ai,bj} = \left(\frac{\partial^2 E}{\partial u^{\mathbf{0}}_{ai} \partial u^{\mathbf{0}}_{bj}} \right) , \tag{J.1}$$

where E denotes the total energy per cell and atoms a and b in the reference cell, with atomic mass M_a and M_b, are displaced along the ith and jth Cartesian directions from the equilibrium configuration. First-order derivatives are computed analytically, whereas second-order derivatives are obtained numerically.[15,16]

The calculation of phonon dispersion was introduced in the CRYSTAL09 version of the program. Beside $\mathbf{W}^{\Gamma}$, a set of dynamical matrices, $\mathbf{W}^{\mathbf{k}}$, need to be defined for a set of wavevectors $\mathbf{k} = \sum_i \frac{\kappa_i}{L_i} \mathbf{b}_i$ expressed as linear combinations of reciprocal lattice basis vectors $\mathbf{b}_i$ with fractional coefficients referred to shrinking factors L_i, κ_i being an integer ranging from 0 to $L_i - 1$, thus including Γ and points within the FBZ. Phonons at $\mathbf{k}$ points other than Γ can be obtained by the *direct method*,[231–234] which requires the construction of supercells (SC) of the original unit cell:

$$W^{\mathbf{k}}_{ai,bj} = \sum_{\mathbf{g} \in SC} \frac{H^{\mathbf{g}}_{ai,bj}}{\sqrt{M_a M_b}} e^{\imath \mathbf{k} \cdot \mathbf{g}} . \tag{J.2}$$

Indeed, equation (J.2) shows that each dynamical matrix in the FBZ is obtained by Fourier transforming the Hessian matrices, $\mathbf{H}^{\mathbf{g}}$, for an adequate set of real space lattice vectors $\mathbf{g}$. Lattice vectors $\mathbf{g} = \sum_i l^g_i \mathbf{a}_i$, expressed in terms of the real lattice basis vectors $\{\mathbf{a}_i\}$ through the integer coefficients l^g_i, are all contained in the SC in real space whose size and shape are determined by parameters L_i. At variance with equation (J.1), the matrix element $H^{\mathbf{g}}_{ai,bj} = \partial^2 E / (\partial u^{\mathbf{0}}_{ai} \partial u^{\mathbf{g}}_{bj})$ refers to a displacement of atom b in cell $\mathbf{g}$ inside the SC along the Cartesian direction j, along with all its images throughout the superlattice generated by the SC. L_i are the same both in the real and the reciprocal space so as to maintain a one-to-one matching between $\mathbf{g}$ vectors in the SC and sampled $\mathbf{k}$ points. From diagonalization of the dynamical matrices the normal modes and corresponding vibration frequencies ($\omega_{\mathbf{k}p}$) are sampled over the entire FBZ.

Knowledge of the full phonon dispersion of a system also allows to compute the phonon density-of-states (PDOS) and to simulate the results of inelastic neutron scattering (INS) experiments. The total PDOS $g(\omega)$ is defined by the equation:

$$g(\omega) = \frac{1}{V_{\mathrm{BZ}}} \int_{\mathrm{BZ}} \sum_{p=1}^{3N} \delta(\omega_{\mathbf{k}p} - \omega) d\mathbf{k} , \tag{J.3}$$

where V_{BZ} is the volume of the Brillouin zone and the integration is performed over it. From equation (J.3), the PDOS is normalized to $3N$, being N the number of atoms per cell ($\int g(\omega) d\omega = 3N$). The total PDOS can be partitioned into atomic contributions $g(\omega) = \sum_a g_a(\omega) x_a$ where the sum runs over the atomic species of the system, x_a is the fraction of atomic species a with respect to N, and

$$g_a(\omega) = \frac{1}{n_{\mathbf{k}}} \sum_{p,\mathbf{k}} |\mathbf{e}_{p,\mathbf{k};a}|^2 \delta(\omega_{\mathbf{k}p} - \omega) , \tag{J.4}$$

where $\mathbf{e}_{p,\mathbf{k}}$ are the eigenvectors of the dynamical matrices $W^{\mathbf{k}}$ defined in equation (J.2) and the integral in equation (J.3) has been replaced by the sum over the sampled points within the FBZ.

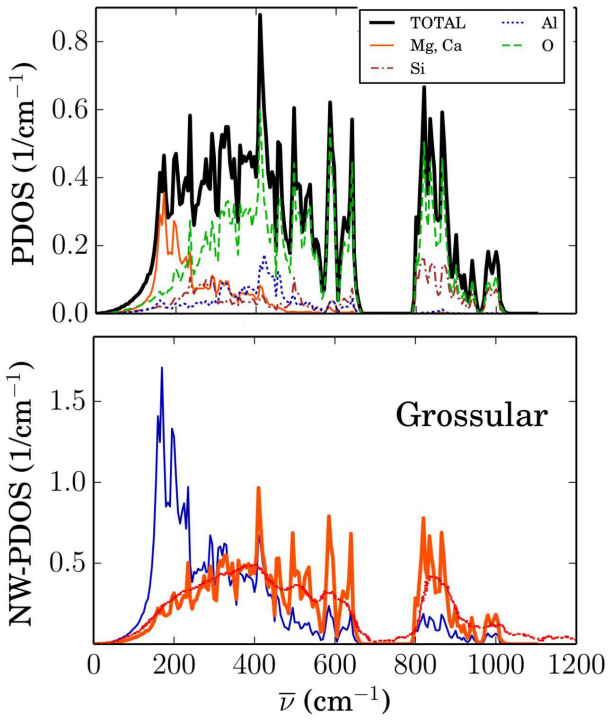

FIG. 11: Upper panel: total (black continuous line) and atomic (dashed green line for O, blue dotted for Al, dark red dot-dashed for Si and continuous red for either Mg or Ca) phonon density-of-states (PDOS) of the grossular silicate garnet, computed on a supercell containing 2160 atoms, with additional $\mathbf{k}$ points obtained by Fourier interpolation (for a overall sampling of phonon dispersion over 13,824 $\mathbf{k}$ points in the FBZ). Lower panel: calculated incoherent (blue thin line) and coherent (thick orange line) neutron-weighted phonon density-of-states (NW-PDOS) for grossular. The experimental coherent INS spectrum is reported in red.[235]

From atomic projected PDOS, a neutron-weighted phonon density-of-states (NW-PDOS) may be defined, which can be compared to the outcomes of INS experiments:

$$g^{\mathrm{NW}}(\omega) = C \sum_a \frac{\sigma_a}{M_a} g_a(\omega) x_a \ , \qquad \text{(J.5)}$$

where C is a normalization factor such that $\int g^{\mathrm{NW}}(\omega) d\omega = 3N$, and the weight of each atomic species a is given by the ratio of the atomic scattering cross-section σ_a and the atomic mass M_a.[236,237] Depending on whether the inelastic scattering is coherent or incoherent, different cross-sections have to be considered, which are tabulated and available on-line.[238,239] In the CRYSTAL17 version of the program, some options have been developed to compute PDOS and NW-PDOS of solids.[27]

As an example, in Figure 11 we report the PDOS and the NW-PDOS of the grossular silicate garnet, $Ca_3Al_2Si_3O_{12}$. In the upper panel, total and atomic projected PDOS are reported, which exhibit the following features:[27] a broad band up to about 700 cm^{-1}, a phonon band-gap of about 120 cm^{-1} and a second, sharper band above approximately 800 cm^{-1} and below about 1100 cm^{-1}. The upper band is seen to be utterly dominated by motions of the SiO_4 tetrahedra. The interesting part of the spectrum (particularly so for thermodynamic properties) is the low-frequency one, which is seen to be mostly affected by the motions of cations in dodecahedral sites (Ca in this case). In the lower panel, we report both the coherent (orange lines) and incoherent (blue lines) NW-PDOS of grossular, as compared with available INS experimental data. A coherent INS spectrum, normalized to $3N$ as in present calculations between 0 and 1100 cm^{-1} (that is, by neglecting the spurious spectral region above 1100 cm^{-1}), was reported for grossular.[235] The agreement is very satisfactory both on peak positions and on the absolute amplitude of the spectral bands.

K. X-ray Diffraction Spectra

X-ray static structure factors F_{hkl} can be computed from the first versions of the program, and correspond to a discrete Fourier transform of the electron charge density of the crystal:

$$F_{hkl} = \int_{\mathrm{cell}} \rho(\mathbf{r}) e^{i2\pi \mathbf{k}\cdot\mathbf{r}} \mathrm{d}\mathbf{r} \ , \qquad \text{(K.1)}$$

where $\mathbf{k} = h\mathbf{b}_1 + k\mathbf{b}_2 + l\mathbf{b}_3$ is a reciprocal lattice vector (being $\mathbf{b}_1$, $\mathbf{b}_2$ and $\mathbf{b}_3$ the fundamental reciprocal lattice vectors) and h,k,l Miller's indices. From the CRYSTAL09 version of the program, Debye-Waller thermal factors can be computed to transform static into dynamical structure factors, starting from harmonic atomic anisotropic displacement parameters (ADPs).[234,240] The intensity of the diffraction peaks is affected by many factors and is proportional to:

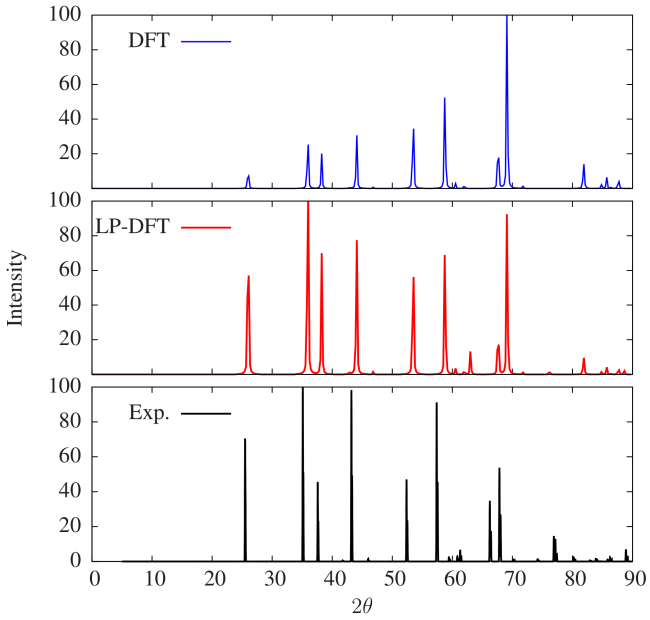

FIG. 12: XRD spectrum of Al_2O_3 Corundum as computed within the DFT with the PBE functional (upper panel), as corrected for Lorentz-polarization factors (middle panel) and as experimentally recorded (lower panel).

$$I_{hkl} \propto |F_{hkl}|^2 \times M_{hkl} \times LP(\theta) \ , \qquad \text{(K.2)}$$

where M_{hkl} is the symmetry multiplicity of the structure factor and $LP(\theta)$ is a correction for Lorentz and Polarization effects, with a functional form depending on Bragg's angle θ (linked to Miller's indices through the spacing of the corresponding crystallographic planes and the wavelength of the experiment). In CRYSTAL17, an option has been implemented, which computes the structure factor multiplicities M_{hkl}, converts h,k,l Miller's indices into Bragg's angle θ, and corrects the intensities for the Lorentz and Polarization (LP) effects. Figure 12 reports the X-ray diffraction spectrum of Al_2O_3 Corundum as experimentally measured (bottom panel), as computed from static structure factors at the PBE level of theory (upper panel), and as computed and corrected for the LP term (middle panel). The LP correction is seen to largely affect relative intensities and to bring the computed spectrum closer to the experimental one.

L. Electronic Transport Properties

Electron transport is a property of primary interest in materials and devices, as it is related to important macroscopic observables such as conductivity (resistivity), the Seebeck effect, thermal conductivity, and many others. The *ab initio* evaluation of the electron transport requires a different treatment according to whether

one considers periodic or non-periodic directions. CRYSTAL17 offers two tools for the above two cases, which we will discuss in the following of this subsection.

1. *Boltzmann Transport Properties*

We are interested in evaluating the three transport coefficients σ (electrical conductivity), S (Seebeck coefficient) and $\kappa_{\rm el}$ (electronic part of the thermal conductivity). According to Boltzmann's semiclassical transport theory,[241] the expressions of the three transport coefficients are obtained (in atomic units) as:

$$[\sigma]_{qr}(\mu,T) = \int \mathrm{d}E\Big(-\frac{\partial f_0}{\partial E}\Big)\Xi_{qr}(E)\;; \tag{L.1}$$

$$[\sigma S]_{qr}(\mu,T) = \frac{1}{T}\int \mathrm{d}E\Big(-\frac{\partial f_0}{\partial E}\Big)(E-\mu)\Xi_{qr}(E) \tag{L.2}$$

$$[\kappa_{el}]_{qr}(\mu,T) = \frac{1}{T}\int \mathrm{d}E\Big(-\frac{\partial f_0}{\partial E}\Big)(E-\mu)^2\Xi_{qr}(E) \tag{L.3}$$

where μ is the chemical potential, T is the temperature, E is the energy, e is the electron charge, f_0 is the Fermi-Dirac distribution and Ξ is the transport distribution function (TDF). In the above equations, the TDF Ξ is defined as:

$$\Xi_{qr}(E) = \tau \sum_{\mathbf{k}} \frac{1}{N_{\mathbf{k}}} \sum_i v_{i,q}(\mathbf{k}) v_{i,r}(\mathbf{k}) \delta\big(E - E_i(\mathbf{k})\big)\;, \tag{L.4}$$

where q and r are Cartesian directions, $v_{i,q}(\mathbf{k})$ is the velocity of the i-th band calculated along the direction q and τ is the lifetime which we assumed to be independent of $\mathbf{k}$ according to the constant relaxation time approximation. The critical quantity that has to be calculated, then, is the band velocity, that along one Cartesian direction q is expressed as the derivative of the band energies $E_i(\mathbf{k})$ with respect to a Cartesian component q of the reciprocal space vector $\mathbf{k}$:

$$v_{i,q}(\mathbf{k}) = \frac{\partial E_i(\mathbf{k})}{\partial k_q} \quad . \tag{L.5}$$

The evaluation of this derivative is not trivial if the wavefunction is expanded in a plane-wave basis set. In fact, approaches developed previously rely either on the interpolation of $\mathbf{k}$-space eigenvalues (e.g. the BoltzTrap[242] program) or localization of the solution (e.g. the BoltzWann[243] program). We have recently implemented[244] in CRYSTAL a novel treatment for such derivatives that allows for an entirely analytical evaluation of band velocities. Thanks to the analytical differentiation, possible problems due to band crossings and/or numerical accuracy of the procedure are avoided.

By differentiating the expression $E_i(\mathbf{k}) = \mathbf{C}_i^\dagger(\mathbf{k})\mathbf{F}(\mathbf{k})\mathbf{C}_i(\mathbf{k})$ with respect to the reciprocal space vector component k_q we obtain:

$$\frac{\partial E_i(\mathbf{k})}{\partial k_q} = \Big[\mathbf{C}^\dagger(\mathbf{k})\frac{\partial \mathbf{F}(\mathbf{k})}{\partial k_q}\mathbf{C}(\mathbf{k})\Big]_{ii} - \Big[\mathbf{C}^\dagger(\mathbf{k})\frac{\partial \mathbf{S}(\mathbf{k})}{\partial k_q}\mathbf{C}(\mathbf{k})\mathbf{E}(\mathbf{k})\Big]_{ii} \quad . \tag{L.6}$$

Note how all the quantities in Eq. (L.6) are directly obtained from the simple SCF HF or DFT solution, apart from $\partial\mathbf{F}(\mathbf{k})/\partial k_q$ and $\partial\mathbf{S}(\mathbf{k})/\partial k_q$, that are however readily computed as a modified Fourier transform of the corresponding direct space quantities

$$\frac{\partial \mathbf{F}(\mathbf{k})}{\partial k_q} = \sum_{\mathbf{g}} i g_q\, \mathbf{F}(\mathbf{g})\; e^{i\mathbf{k}\cdot\mathbf{g}}\;;\; \frac{\partial \mathbf{S}(\mathbf{k})}{\partial k_q} = \sum_{\mathbf{g}} i g_q\, \mathbf{S}(\mathbf{g})\; e^{i\mathbf{k}\cdot\mathbf{g}}\;. \tag{L.7}$$

In Figure 13 we show how the abovementioned transport coefficients (Equations L.1 – L.3) are computed by

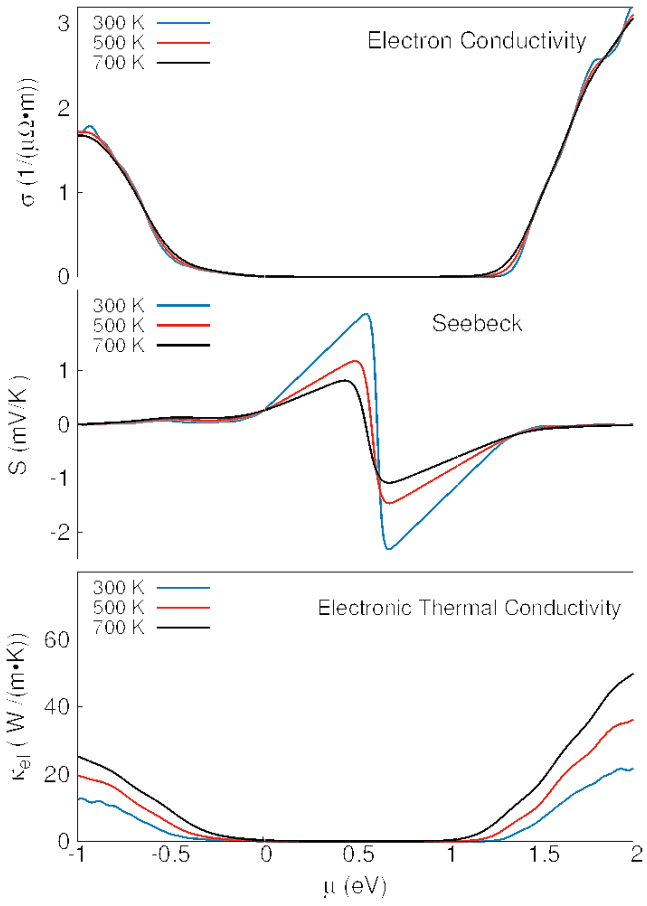

FIG. 13: Transport properties of cubic $CoSb_3$ skutterodite crystal evaluated at the PBE0 level at three different temperatures as a function of chemical potential. Plotted values are tensor elements along principal direction xx ≡ yy ≡ zz; others are null. The zero of the potential is set at the Fermi level, defined as the top of conduction bands. For other details see text.

CRYSTAL17 for the $CoSb_3$ crystal.[244] Calculations are performed at the PBE0 level, using an [ECP:8811s-661p-61d] basis set on antimonium and an all electron [6s-6631sp-31d-1f] basis on cobalt, as described in the supplementary information of Ref. 156. Gaussian smearing is applied.

Cobalt antimonide (cubic $Im\bar{3}$ space group) is a prototypical thermoelectric material. A high sensitivity of the Seebeck coefficient to temperature is the main indicator of the thermoelectric behavior, and it is evident from the middle panel of Fig. 13 that our simulation fully reproduces such sensitivity. As $CoSb_3$ is an insulator, at low applied voltage – that is, at values of μ immediately above the Fermi level – the electrical conductivity is null. Nevertheless, above 1.3 eV (corresponding to the band gap, and thus to the estimated breakdown voltage), conductivity ramps up quickly. In a frozen band approximation, this information can be also correlated to the conductivity of the material at a given doping level (that is, assuming that in the material permanently contains a number of carriers having energy in the conduction band). Our results in Figure 13 and those in Ref. 244 can be directly compared to those obtained by other approaches,[242,243] showing excellent agreement despite the different basis set – that is a plane wave one in those cases.

We underline that our analytical approach has no problems with band crossings, since the local basis set allows to exploit the shortsightedness of the Fock operator. As a consequence, it can be straightforwardly applied to conducting systems as well (in Ref. 244 the case of graphene is reported). As in all properties directly related to the electronic band structure, the use of hybrid functional is highly recommended, as an accurate description of band gaps is key to reliable electronic transport results.

2. *Transport across Nano-junctions*

In the emerging field of molecular electronics, the goal is to create devices based on electronic current passing through one or more molecules connecting metal leads (such as in the lead-conductor-lead configuration of the nano-junction sketched in Figure 14). Assuming that the Fermi level of the metal leads, E_F, lies between the HOMO and LUMO electronic states of the bridging molecule, the application of a small voltage results in electron transport through the molecule via non-resonant tunneling.

The tunneling probability is quantified by the so called β parameter. For each energy E of the scattering electrons, the $\beta(E)$ curve gives a simple quantitative measure of the decay rate (in the insulating central region) of the wavefunctions carrying the tunneling current and so reveals the expected dependence of the current flowing through the junction as a function of the junction length L:

$$I = I_0 \exp(-\beta L) \; . \tag{L.8}$$

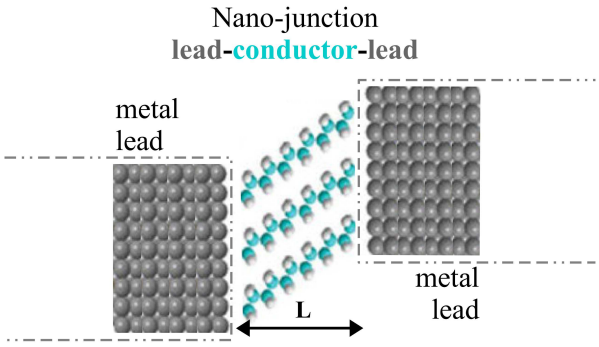

FIG. 14: Schematic representation of a lead-conductor-lead nano-junction, where the conductor layer (of thickness L) is constituted by organic molecules.

The tunneling electrons are those located near or at E_F, so, in order to understand electron transport through the nano-junction, it is necessary to estimate where E_F lies relatively to the insulator energy levels.

The complex band structure approach (CBS) proposed by Tomfohr and Sankey,[245] provides a clear picture of the nature of the electron states in the gap region of a molecule. Within this approach, the CBS has to be evaluated in the limit of an infinitely thick insulating region and the outcome of this procedure is a set of $\beta(E)$ curves. The value β_0 to be compared with the experiments is the smallest one aligned with the Fermi level of the junction

$$\beta_0 \; = \; \beta(E_F) \; . \tag{L.9}$$

The Fermi level alignment is not computed explicitly but it can be roughly estimated by evaluating $\beta(E)$ at the energy where $d\beta/dE = 0$, the so called branch point. This method is originally due to Tersoff and is based on the pinning of E_F by metal-induced gap states.[246] A direct evaluation of the Fermi level alignment is also possible (and in some cases needed) but requires an explicit calculation for the insulator plus metal leads systems.

In principle, the β_0 parameter also depends on the atomistic details at the lead-conductor interface, but it mostly embodies the properties of the tunneling layer itself, which allows for its evaluation from a single quantum-mechanical calculation of the infinite molecular chain (i.e. polymer) within the CBS theory. Such a calculation can easily be performed with the CRYSTAL program. The whole CBS procedure is implemented in the WANT code,[247] which has been conveniently interfaced to CRYSTAL17. An application of such a scheme to various conjugated polymers has recently been reported.[248]

III. CONCLUSIONS

An overview of the functionalities of the publicly distributed CRYSTAL17 program for the quantum-mechanical simulation of physical and chemical proper-

ties of condensed matter has been presented. In particular, the new features of the code with respect to the previous major release, namely CRYSTAL14, include: i) implementation of a DIIS scheme for SCF and CPHF/KS convergence acceleration (now active by default); ii) fully-automated implementation of the quasi-harmonic approximation for volume-dependent thermal properties; iii) input parameter-free implementation of Grimme's DFT-D3 correction for weak dispersive interactions as well as a semiempirical composite method for molecular crystals; iv) calculation of elastic constants under pressure, directional elastic wave velocities, the piezo-optic tensor, and the piezoelectric tensor through an analytical CPHF/KS approach; v) calculation of dynamic linear polarizabilities, second harmonic generation and Pockels effect; vi) self-consistent system-specific hybrid functionals; vii) improved scalability of the massively-parallel version of the program, MPPCRYSTAL; viii) implementation of new tools for magnetic systems (evaluation of spin contamination, restricted open-shell Hartree-Fock, and non-integer spin locking); ix) atomic partition of the electron charge density according to the Hirshfeld-I scheme; x) calculation of total and projected phonon density-of-states as well as its neutron-weighted counterpart (for simulation of inelastic neutron scattering); xi) calculation of X-ray diffraction spectra; and xii) evaluation of several electronic transport properties (electrical conductivity, Seebeck coefficient, electronic contribution to thermal conductivity and transport across nanojunctions).

The CRYSPLOT web-oriented application has also been developed (available at http://crysplot.crystalsolutions.eu) for the graphical representation and plotting of most properties of solids computed by the CRYSTAL program. The application has been designed with the advanced graphical javascript library `Plotly` and allows data to be easily read from output files generated by CRYSTAL.

Acknowledgments

This work is dedicated to the memory of Claudio M. Zicovich-Wilson and Roberto Orlando for their countless contributions to the development of the CRYSTAL program and for being our friends in the last 30 years.

* Electronic address: `alessandro.erba@unito.it`

[1] J. Hafner, C. Wolverton, and G. Ceder, MRS Bulletin **31**, 659 (2006).
[2] J. Landers, G. Y. Gor, and A. V. Neimark, Colloids and Surfaces A: Physicochem. Eng. Aspects **437**, 3 (2013).
[3] A. Jain, G. Hautier, C. J. Moore, S. P. Ong, C. C. Fischer, T. Mueller, K. A. Persson, and G. Ceder, Comput. Mater. Sci. **50**, 2295 (2011).
[4] R. Dovesi, R. Orlando, A. Erba, C. M. Zicovich-Wilson, B. Civalleri, S. Casassa, L. Maschio, M. Ferrabone, M. De La Pierre, Ph. D'Arco, et al., Int. J. Quantum Chem. **114**, 1287 (2014).
[5] C. Pisani, R. Dovesi, and C. Roetti, *Hartree-Fock Ab Initio Treatment of Crystalline solids*, vol. 48 of *Lecture Notes in Chemistry Series* (Springer Verlag, Berlin, 1988).
[6] R. Dovesi, Int. J. Quantum Chem. **29**, 1755 (1986).
[7] C. Zicovich-Wilson and R. Dovesi, Int. J. Quantum Chem. **67**, 299 (1998).
[8] C. Zicovich-Wilson and R. Dovesi, Int. J. Quantum Chem. **67**, 311 (1998).
[9] P. Pulay, Chem. Phys. Lett. **73**, 393 (1980), ISSN 0009-2614.
[10] P. Pulay, J. Comput. Chem. **3**, 556 (1982), ISSN 1096-987X.
[11] D. D. Johnson, Phys. Rev B **38**, 12807 (1988).
[12] D. G. Anderson, J. Assoc. Comput. Mach. **12**, 547 (1965).
[13] G. Kresse and J. Furthmüller, Phys. Rev. B **54**, 11169 (1996).
[14] L. Maschio, Submitted to J. Comput. Chem. (2017).
[15] F. Pascale, C. M. Zicovich-Wilson, F. L. Gejo, B. Civalleri, R. Orlando, and R. Dovesi, J. Comp. Chem. **25**, 888 (2004).
[16] C. M. Zicovich-Wilson, F. Pascale, C. Roetti, V. R. Saunders, R. Orlando, and R. Dovesi, J. Comp. Chem. **25**, 1873 (2004).
[17] F. Pascale, C. M. Zicovich-Wilson, R. Orlando, C. Roetti, P. Ugliengo, and R. Dovesi, J. Phys. Chem. B **109**, 6146 (2005).
[18] C. Carteret, M. De La Pierre, M. Dossot, F. Pascale, A. Erba, and R. Dovesi, J. Chem. Phys. **138**, 014201 (2013).
[19] A. Erba, S. Casassa, R. Dovesi, L. Maschio, and C. Pisani, J. Chem. Phys. **130**, 074505 (2009).
[20] L. Maschio, B. Kirtman, M. Rérat, R. Orlando, and R. Dovesi, J. Chem. Phys. **139**, 167101 (2013).
[21] L. Maschio, B. Kirtman, M. Rérat, R. Orlando, and R. Dovesi, J. Chem. Phys. **139**, 164101 (2013).
[22] L. Maschio, B. Kirtman, M. Rérat, R. Orlando, and R. Dovesi, J. Chem. Phys. **139**, 164102 (2013).
[23] L. Maschio, B. Kirtman, S. Salustro, C. M. Zicovich-Wilson, R. Orlando, and R. Dovesi, J. Phys. Chem. A **117**, 11464 (2013).
[24] M. De La Pierre, C. Carteret, L. Maschio, E. André, R. Orlando, and R. Dovesi, J. Chem. Phys. **140**, 164509 (2014).
[25] M. Prencipe, L. Maschio, B. Kirtman, S. Salustro, A. Erba, and R. Dovesi, J. Raman Spectrosc. **45**, 703 (2014).
[26] J. Maul, A. Erba, I. M. G. Santos, J. R. Sambrano, and R. Dovesi, J. Chem. Phys. **142**, 014505 (2015).
[27] J. Baima, M. Ferrabone, R. Orlando, A. Erba, and R. Dovesi, Phys. Chem. Minerals **43**, 137 (2016).
[28] N. W. Ashcroft and N. D. Mermin, *Solid State Physics* (Saunders College, Philadelphia, USA, 1976).
[29] S. Baroni, P. Giannozzi, and E. Isaev, Reviews in Mineralogy and Geochemistry **71**, 39 (2010).

[30] R. E. Allen and F. W. De Wette, Phys. Rev. **179**, 873 (1969).
[31] L. L. Boyer, Phys. Rev. Lett. **42**, 584 (1979).
[32] A. Erba, J. Maul, R. Demichelis, and R. Dovesi, Phys. Chem. Chem. Phys. **17**, 11670 (2015).
[33] D. C. Wallace, *Thermodynamics of Crystals* (Wiley, New York, USA, 1972).
[34] S. Q. Wang, Appl. Phys. Lett. **88**, 061902 (2006).
[35] S. Schmerler and J. Kortus, Phys. Rev. B **89**, 064109 (2014).
[36] B. B. Karki, R. M. Wentzcovitch, S. de Gironcoli, and S. Baroni, Phys. Rev. B **61**, 8793 (2000).
[37] Y. Wang, J. J. Wang, H. Zhang, V. R. Manga, S. L. Shang, L.-Q. Chen, and Z.-K. Liu, J. Phys.: Cond. Matter **22**, 225404 (2010).
[38] S.-L. Shang, H. Zhang, Y. Wang, and Z.-K. Liu, J. Phys.: Cond. Matter **22**, 375403 (2010).
[39] A. Erba, J. Chem. Phys. **141**, 124115 (2014).
[40] A. Erba, M. Shahrokhi, R. Moradian, and R. Dovesi, J. Chem. Phys. **142**, 044114 (2015).
[41] A. Erba, J. Maul, M. De La Pierre, and R. Dovesi, J. Chem. Phys. **142**, 204502 (2015).
[42] S. Ganesan, Philosophical Magazine **7**, 197 (1962).
[43] O. L. Anderson, D. Isaak, and H. Oda, Rev. Geophys. **30**, 57 (1992).
[44] G. K. White and O. L. Anderson, J. Appl. Phys. **37**, 430 (1966).
[45] B. B. Karki and R. M. Wentzcovitch, Phys. Rev. B **68**, 224304 (2003).
[46] A. Erba, J. Maul, M. Itou, R. Dovesi, and Y. Sakurai, Phys. Rev. Lett. **115**, 117402 (2015).
[47] J. Maul, I. M. G. Santos, J. R. Sambrano, and A. Erba, Theor. Chem. Acc. **135**, 1 (2016).
[48] A. Erba, J. Maul, and B. Civalleri, Chem. Commun. **52**, 1820 (2016).
[49] M. T. Ruggiero, J. Zeitler, and A. Erba, Chem. Commun. **53**, 3781 (2017).
[50] J. G. Brandenburg, J. Potticary, H. A. Sparkes, S. L. Price, and S. R. Hall, J. Phys. Chem. Lett. **8**, 4319 (2017).
[51] S. Grimme, A. Hansen, J. G. Brandenburg, and C. Bannwarth, Chem. Rev. **116**, 5105 (2016).
[52] J. Klimes and A. Michaelides, J. Chem. Phys. **137**, 120901 (2012).
[53] S. Grimme, J. Chem. Theory Comput. **27**, 1787 (2006).
[54] B. Civalleri, C. M. Zicovich-Wilson, L. Valenzano, and P. Ugliengo, CrystEngComm **10**, 405 (2008).
[55] S. Grimme, J. Antony, S. Ehrlich, and H. Krieg, J. Chem. Phys. **132**, 154104 (2010).
[56] H. Kruse and S. Grimme, J. Chem. Phys. **136**, 154101 (2012).
[57] S. F. Boys and F. Bernardi, Mol. Phys. **19**, 553 (1970).
[58] R. Sure and S. Grimme, J. Chem. Theory Comput. **34**, 16721685 (2013).
[59] R. Sure, J. G. Brandenburg, and S. Grimme, ChemistryOpen **5**, 94 (2016).
[60] S. Grimme, J. G. Brandenburg, C. Bannwarth, and A. Hansen, J. Chem. Phys. **143**, 054107 (2015).
[61] F. Weigend and R. Ahlrichs, Phys. Chem. Chem. Phys. **7**, 3297 (2005).
[62] J. G. Brandenburg and S. Grimme, *Dispersion Corrected HartreeFock and Density Functional Theory for Organic Crystal Structure Prediction* (Springer, Cambridge, 2013), pp. 1–24, In Prediction and Calculation of Crystal Structures. Methods and Applications, s. atahan-evrenk and a. aspuru-guzik ed.
[63] J. G. Brandenburg and S. Grimme, Top. Curr. Chem. **345**, 1 (2013).
[64] J. G. Brandenburg, M. Alessio, B. Civalleri, M. F. Peintinger, T. Bredow, and S. Grimme, J. Phys. Chem. A **117**, 9282 (2013).
[65] M. Cutini, B. Civalleri, M. Corno, R. Orlando, J. G. Brandenburg, L. Maschio, and P. Ugliengo, J. Comp. Chem. **12**, 3340 (2016).
[66] A. Otero-De-La-Roza and E. R. Johnson, J. Chem. Phys. **137**, 054103 (2012).
[67] A. M. Reilly and A. Tkatchenko, J. Chem. Phys. **139**, 024705 (2013).
[68] R. D. King-Smith and D. Vanderbilt, Phys. Rev. B **47**, 1651 (1993).
[69] D. Vanderbilt, J. Phys. Chem. Solids **61**, 147 (2000).
[70] R. Resta, Rev. Mod. Phys. **66**, 899 (1994).
[71] A. Erba, K. E. El-Kelany, M. Ferrero, I. Baraille, and M. Rérat, Phys. Rev. B **88**, 035102 (2013).
[72] A. Mahmoud, A. Erba, K. E. El-Kelany, M. Rérat, and R. Orlando, Phys. Rev. B **89**, 045103 (2014).
[73] J. Baima, A. Erba, R. Orlando, M. Rérat, and R. Dovesi, J. Phys. Chem. C **117**, 12864 (2013).
[74] K. E. El-Kelany, P. Carbonnière, A. Erba, and M. Rérat, J. Phys. Chem. C **119**, 8966 (2015).
[75] K. E. El-Kelany, P. Carbonnière, A. Erba, J.-M. Sotiropoulos, and M. Rérat, J. Phys. Chem. C **120**, 7795 (2016).
[76] B. B. Karki, L. Stixrude, and R. M. Wentzcovitch, Rev. Geophys. **39**, 507 (2001).
[77] W. F. Perger, J. Criswell, B. Civalleri, and R. Dovesi, Comput. Phys. Commun. **180**, 1753 (2009).
[78] A. Erba, A. Mahmoud, R. Orlando, and R. Dovesi, Phys. Chem. Miner. **41**, 151 (2014).
[79] A. Zoroddu, F. Bernardini, P. Ruggerone, and V. Fiorentini, Phys. Rev. B **64**, 045208 (2001).
[80] R. Golesorkhtabar, P. Pavone, J. Spitaler, P. Puschnig, and C. Draxl, Comp. Phys. Commun. **184**, 1861 (2013).
[81] V. Milman and M. C. Warren, J. Phys.: Condens Matter **13**, 5585 (2001).
[82] D. Donadio, M. Bernasconi, and F. Tassone, Phys. Rev. B **68**, 134202 (2003).
[83] F. Detraux and X. Gonze, Phys. Rev. B **63**, 115118 (2001).
[84] A. Erba and R. Dovesi, Phys. Rev. B **88**, 045121 (2013).
[85] A. Erba, M. T. Ruggiero, T. M. Korter, and R. Dovesi, J. Chem. Phys. **143**, 144504 (2015).
[86] B. Mytsyk, A. Erba, N. Demyanyshyn, and A. Saharuk, Opt. Mater. **62**, 632 (2016).
[87] X. Wu, D. Vanderbilt, and D. R. Hamann, Phys. Rev. B **72**, 035105 (2005).
[88] M. Veithen, X. Gonze, and P. Ghosez, Phys. Rev. B **71**, 125107 (2005).
[89] R. Yu, J. Zhu, and H. Ye, Comp. Phys. Commun. **181**, 671 (2010).
[90] A. Erba, D. Caglioti, C. M. Zicovich-Wilson, and R. Dovesi, J. Comput. Chem. **38**, 257 (2017).
[91] A. Erba, M. Ferrabone, J. Baima, R. Orlando, M. Rérat, and R. Dovesi, J. Chem. Phys. **138**, 054906 (2013).
[92] B. B. Karki, G. J. Ackland, and J. Crain, J. Phys.: Cond. Matter **9**, 8579 (1997).
[93] J. Wang, J. Li, S. Yip, S. Phillpot, and D. Wolf, Phys. Rev. B **52**, 12627 (1995).
[94] D. C. Wallace, Rev. Mod. Phys. **37**, 57 (1965).

[95] A. Erba, A. Mahmoud, D. Belmonte, and R. Dovesi, J. Chem. Phys. **140**, 124703 (2014).
[96] A. Mahmoud, A. Erba, K. Doll, and R. Dovesi, J. Chem. Phys. **140**, 234703 (2014).
[97] A. Erba, A. M. Navarrete-López, V. Lacivita, P. D'Arco, and C. M. Zicovich-Wilson, Phys. Chem. Chem. Phys. **17**, 2660 (2015).
[98] V. Lacivita, A. Erba, R. Dovesi, and Ph. D'Arco, Phys. Chem. Chem. Phys. **16**, 15331 (2014).
[99] K. Doll, Molecular Physics **108**, 223 (2010).
[100] K. Doll, R. Dovesi, and R. Orlando, Theor. Chem. Acc. **112**, 394 (2004).
[101] K. Doll, R. Dovesi, and R. Orlando, Theor. Chem. Acc. **115**, 354 (2006).
[102] J. F. Nye, *Physical properties of crystals* (Oxford University Press, Oxford, 1957).
[103] M. J. P. Musgrave, *Crystal Acoustics* (Holden-Day, San Francisco, California, 1970).
[104] B. A. Auld, *Acoustic Fields and Waves in Solids* (Krieger Publishing Company, Malabar, Florida, 1973).
[105] D. Muñoz-Santiburcio, A. Hernández-Laguna, and J. I. Soto, Comput. Phys. Commun. **192**, 272 (2015).
[106] D. Muñoz-Santiburcio and A. Hernández-Laguna, Comput. Phys. Commun. **217**, 212 (2017).
[107] M. Catti, Y. Noël, and R. Dovesi, J. Phys. Chem. Solids **64**, 2183 (2003).
[108] Y. Noël, M. Llunell, R. Orlando, Ph. D'Arco, and R. Dovesi, Phys. Rev. B **66**, 214107 (2002).
[109] J. Baima, A. Erba, L. Maschio, C. Zicovich-Wilson, R. Dovesi, and B. Kirtman, Z. Phys. Chem. **230**, 719 (2016).
[110] A. Erba, Phys. Chem. Chem. Phys. **18**, 13984 (2016).
[111] G. Saghi-Szabo, R. E. Cohen, and H. Krakauer, Phys. Rev. Lett. **80**, 4321 (1998).
[112] A. Dal Corso, M. Posternak, R. Resta, and A. Baldereschi, Phys. Rev. B **50**, 10715 (1994).
[113] D. R. Hamann, X. Wu, K. M. Rabe, and D. Vanderbilt, Phys. Rev. B **71**, 035117 (2005).
[114] P. Pulay, Mol. Phys. **17**, 197 (1969).
[115] H.-J. Weber, Phys. Rev. B **51**, 12209 (1995).
[116] O. Krupych, V. Savaryn, A. Krupych, I. Klymiv, and R. Vlokh, Appl. Opt. **52**, 4054 (2013).
[117] T. S. Narasimhamurty, *Photoelastic and Electrooptic Properties of Crystals* (Plenum, 1981).
[118] I. Slezinger, A. Alievskaya, and Y. Mironov, Measur. Tech. **28**, 1059 (1985).
[119] J. Badoz, M. Billardon, J. C. Canit, and M. F. Russel, Journal of Optics **8**, 373 (1977).
[120] J. C. Kemp, J. Opt. Soc. Am. **59**, 950 (1969).
[121] J. Xu and R. Stroud, *Acousto-Optic Devices: Principles, Design, and Applications* (Wiley, 1992).
[122] A. S. Andrushchak, B. G. Mytsyk, H. P. Laba, O. V. Yurkevych, I. M. Solskii, A. V. Kityk, and B. Sahraoui, J. Appl. Phys. **106** (2009).
[123] B. G. Mytsyk, A. S. Andrushchak, N. M. Demyanyshyn, Y. P. Kost', A. V. Kityk, P. Mandracci, and W. Schranz, Appl. Opt. **48**, 1904 (2009).
[124] B. Mytsyk, V. Shut, N. Demyanyshyn, S. Mozzharov, A. Erba, B. Kalynyak, O. Mys, and R. Vlokh, Ukr. J. Phys. Opt. **18**, 46 (2017).
[125] G. Hurst, M. Dupuis, and E. Clementi, J. Chem. Phys. **89**, 385 (1988).
[126] B. Kirtman, F. L. Gu, and D. M. Bishop, J. Chem. Phys. **113**, 1294 (2000).
[127] P. Otto, Phys. Rev. B **45**, 10876 (1992).
[128] B. Champagne, J. G. Fripiat, and J. André, J. Chem. Phys. **96**, 8330 (1992).
[129] P. Otto, F. L. Gu, and J. Ladik, J. Chem. Phys. **110**, 2717 (1999).
[130] M. Ferrero, M. Rérat, R. Orlando, and R. Dovesi, J. Comp. Chem. **29**, 1450 (2008).
[131] M. Ferrero, M. Rérat, R. Orlando, and R. Dovesi, J. Chem. Phys. **128**, 014110 (2008).
[132] M. Ferrero, M. Rérat, R. Orlando, R. Dovesi, and I. Bush, *In Ab Initio Simulation of Crystalline Solids: History and Prospects*, vol. 117 (Dovesi R., Roetti C. and Orlando R. Editors, IOP Publishing, Bristol, UK, 2008).
[133] R. Orlando, M. Ferrero, M. Rérat, B. Kirtman, and R. Dovesi, J. Chem. Phys. **131**, 184105 (2009).
[134] L. Maschio, B. Kirtman, R. Orlando, and M. Rérat, J. Chem. Phys. **137**, 204113 (2012).
[135] L. Bernasconi, S. Tomić, M. Ferrero, M. Rérat, R. Orlando, R. Dovesi, and N. M. Harrison, Phys. Rev. B **83**, 195325 (2011).
[136] B. J. Orr and J. F. Ward, Mol. Phys. **20**, 513 (1971).
[137] D. M. Bishop and B. Kirtman, J. Chem. Phys. **95**, 2646 (1991).
[138] J. E. Rice, R. D. Amos, S. M. Colwell, N. C. Handy, and J. Sanz, J. Chem. Phys. **93**, 8828 (1990).
[139] S. P. Karna and M. Dupuis, J. Comp. Chem. **12**, 487 (1991).
[140] A. M. Ferrari, R. Orlando, and M. Rérat, J. Chem. Theor. Comput. **11**, 3245 (2015).
[141] M. Ferrero, M. Rérat, B. Kirtman, and R. Dovesi, J. Chem. Phys. **129**, 244110 (2008).
[142] B. Kirtman, F. L. Gu, and D. M. Bishop, J. Chem. Phys. **45**, 1294 (2000).
[143] M. Rérat, L. Maschio, B. Kirtman, B. Civalleri, and R. Dovesi, J. Chem. Theory Comput. **12**, 107 (2016).
[144] L. Maschio, M. Rérat, B. Kirtman, and R. Dovesi, J. Chem. Phys. **143**, 244102 (2015).
[145] R. Orlando, V. Lacivita, R. Bast, and K. Ruud, J. Chem. Phys. **132**, 244106 (2010).
[146] S. Kümmel and L. Kronik, Rev. Mod. Phys. **80**, 3 (2008).
[147] A. D. Becke, J. Chem. Phys. **98**, 5648 (1993).
[148] W. Koch and M. C. Holthausen, *A Chemists Guide to Density Functional Theory* (Wiley-VCH, Heidelberg, 2001).
[149] O. B. Lutnaes, T. A. Ruden, and T. Helgaker, Magnetic Resonance in Chemistry **42**, S117 (2004).
[150] P. E. M. Siegbahn, J. Biol. Inorg. Chem. **11**, 695 (2006).
[151] S. Kossmann, B. Kirchner, and F. Neese, Mol. Phys. **105**, 2049 (2007).
[152] M. D. Halls and H. B. Schlegel, J. Chem. Phys. **109**, 10587 (1998).
[153] F. Furche and J. P. Perdew, J. Chem. Phys. **124**, 044103 (2006).
[154] F. Corà, M. Alfredsson, G. Mallia, D. S. Middlemiss, W. C. Mackrodt, R. Dovesi, and R. Orlando, *The Performance of Hybrid Density Functionals in Solid State Chemistry* (Springer Berlin Heidelberg, Berlin, Heidelberg, 2004), pp. 171–232.
[155] F. Corá, Mol. Phys. **103**, 2483 (2005).
[156] J. M. Crowley, J. Tahir-Kheli, and W. A. Goddard, J. Phys. Chem. Lett. **7**, 1198 (2016).
[157] R. Wahl, D. Vogtenhuber, and G. Kresse, Phys. Rev. B **78**, 104116 (2008).
[158] J. Heyd and G. E. Scuseria, J. Chem. Phys. **121**, 1187

(2004).
[159] J. Paier, M. Marsman, K. Hummer, G. Kresse, I. C. Gerber, and J. G. Angyan, J. Chem. Phys. **124**, 154709 (2006).
[160] M. Marsman, J. Paier, A. Stroppa, and G. Kresse, J. Phys.: Cond. Matt. **20**, 064201 (2008).
[161] B. G. Janesko, T. M. Henderson, and G. E. Scuseria, Phys. Chem. Chem. Phys. **11**, 443 (2009).
[162] R. Dovesi, C. Pisani, C. Roetti, and V. R. Saunders, Phys. Rev. B **28**, 5781 (1983).
[163] R. Colle and O. Salvetti, Theor. Chem. Acc. **37**, 329 (1975).
[164] M. Causà, R. Dovesi, C. Pisani, R. Colle, and A. Fortunelli, Phys. Rev. B **36**, 891 (1987).
[165] M. D. Towler, A. Zupan, and M. Causá, Comput. Phys. Commun. **98**, 181 (1996).
[166] C. Adamo and V. Barone, J. Chem. Phys. **110**, 6158 (1999).
[167] J. Heyd, G. E. Scuseria, and M. Ernzerhof, J. Chem. Phys. **124**, 219906 (2006).
[168] D. I. Bilc, R. Orlando, R. Shaltaf, G.-M. Rignanese, J. Íñiguez, and P. Ghosez, Phys. Rev. B **77**, 165107 (2008).
[169] M. A. L. Marques, J. Vidal, M. J. T. Oliveira, L. Reining, and S. Botti, Phys. Rev. B **83**, 035119 (2011).
[170] A. Alkauskas, P. Broqvist, and A. Pasquarello, Phys. Status Solidi B **248**, 775 (2011).
[171] J. Conesa, J. Phys. Chem. C **116**, 18884 (2012).
[172] J. E. Moussa, P. A. Schultz, and J. R. Chelikowsky, J. Chem. Phys. **136**, 204117 (2012).
[173] T. Shimazaki and T. Nakajima, J. Chem. Phys. **141**, 114109 (2014).
[174] Z.-h. Yang, F. Sottile, and C. A. Ullrich, Phys. Rev. B **92**, 035202 (2015).
[175] J. H. Skone, M. Govoni, and G. Galli, Phys. Rev. B **89**, 195112 (2014).
[176] M. Gerosa, C. E. Bottani, L. Caramella, G. Onida, C. Di Valentin, and G. Pacchioni, Phys. Rev. B **91**, 155201 (2015).
[177] E. Menéndez-Proupin, P. Palacios, P. Wahnón, and J. C. Conesa, Phys. Rev. B **90**, 045207 (2014).
[178] J. M. Morbec, I. Narkeviciute, T. F. Jaramillo, and G. Galli, Phys. Rev. B **90**, 155204 (2014).
[179] G. Pacchioni, Catal. Lett. **145**, 80 (2015).
[180] M. Gerosa, C. E. Bottani, L. Caramella, G. Onida, C. D. Valentin, and G. Pacchioni, J. Chem. Phys. **143**, 134702 (2015).
[181] H. Jiang, Int. J. Quantum Chem. **115**, 722 (2015).
[182] A. P. Gaiduk, M. Govoni, R. Seidel, J. H. Skone, B. Winter, and G. Galli, J. Am. Chem. Soc. **138**, 6912 (2016).
[183] A. M. Ferrari, R. Orlando, and M. Rrat, J. Chem. Theor. Comput. **11**, 3245 (2015).
[184] M. Gerosa, C. D. Valentin, C. E. Bottani, G. Onida, and G. Pacchioni, J. Chem. Phys. **143**, 111103 (2015).
[185] A. Bankura, B. Santra, R. A. D. Jr., C. W. Swartz, M. L. Klein, and X. Wu, Mol. Phys. **113**, 2842 (2015).
[186] A. Erba, J. Phys.: Condens. Matter **29**, 314001 (2017).
[187] T. Tsuneda and K.Hirao, WIREs Comput. Mol. Sci. **4**, 375 (2014).
[188] A. Savin, J. Toulouse and H. J. Flad, Int. J. Quantum Chem. **100**, 1047 (2004).
[189] I. C. Gerber, J. G. Angyan, M. Marsman and Kresse G., J. Chem. Phys. **127**, 054101 (2007).
[190] Jeng-Da Chai and M. Head-Gordon, J. Chem. Phys. **128**, 084106 (2008).
[191] H. Iikura, T. Tsuneda, T. Yanai, and K. Hirao, J. Chem. Phys. **115**, 3540 (2001).
[192] Y. Tawada, T. Tsuneda, S. Yanagisawa, T. Yanai, and K. Hirao, J. Chem. Phys. **120**, 8425 (2004).
[193] T. Yanai, D. P. Tew, and N. C. Handy, Chem. Phys. Lett. **393**, 51 (2004).
[194] N. Otero, P. Karamanis, K. E. El-Kelany, M. Rerat, L. Maschio, B. Civalleri, and B. Kirtman, J. Phys. Chem. C **121**, 709 (2017).
[195] S. Salustro, L. Maschio, B. Kirtman, M. Rrat, and R. Dovesi, J. Phys. Chem. C **120**, 6756 (2016).
[196] R. Dovesi, B. Civalleri, R. Orlando, C. Roetti, and V. R. Saunders, Rev. Comp. Chem. **21**, 1 (2005).
[197] R. Orlando, M. De La Pierre, C. M. Zicovich-Wilson, A. Erba, and R. Dovesi, J. Chem. Phys. **141**, 104108 (2014).
[198] S. Casassa, A. Erba, J. Baima, and R. Orlando, J. Comput. Chem. **36**, 1940 (2015).
[199] I. J. Bush, S. Tomic, B. G. Searle, G. Mallia, C. L. Bailey, B. Montanari, L. Bernasconi, J. M. Carr, and N. M. Harrison, Proc. R. Soc. A: Math. Phys. Eng. Sci **467**, 2112 (2011).
[200] R. Orlando, M. Delle Piane, I. J. Bush, P. Ugliengo, M. Ferrabone, and R. Dovesi, J. Comput. Chem. **33**, 2276 (2012).
[201] A. Erba, J. Baima, I. Bush, R. Orlando, and R. Dovesi, J. Chem. Theory Comput. (2017), submitted.
[202] G. M. Amdahl, in *Proceedings of the April 18-20, 1967, Spring Joint Computer Conference* (ACM, New York, NY, USA, 1967), AFIPS '67 (Spring), pp. 483–485.
[203] Y. Noel, M. De La Pierre, C. M. Zicovich-Wilson, R. Orlando, and R. Dovesi, Phys. Chem. Chem. Phys. **16**, 13390 (2014).
[204] S. Salustro, A. Ferrari, R. Orlando, and R. Dovesi, Theor. Chem. Acc. (2017), in press.
[205] J. Baima, A. Zelferino, P. Olivero, A. Erba, and R. Dovesi, Phys. Chem. Chem. Phys. **18**, 1961 (2016).
[206] S. Salustro, A. Erba, C. Zicovich-Wilson, Y. Nöel, L. Maschio, and R. Dovesi, Phys. Chem. Chem. Phys. **18**, 21288 (2016).
[207] R. Demichelis, M. De La Pierre, M. Mookherjee, C. M. Zicovich-Wilson, and R. Orlando, CrystEngComm **18**, 4412 (2016).
[208] G. Sansone, L. Maschio, and A. Karttunen, Chem. Eur. J. (2017).
[209] M. Delle Piane, M. Corno, R. Orlando, R. Dovesi, and P. Ugliengo, Chem. Sci. **7**, 1496 (2016).
[210] M. Delle Piane, M. Corno, A. Pedone, R. Dovesi, and P. Ugliengo, J. Phys. Chem. C **118**, 26737 (2014).
[211] B. Civalleri (2017), in preparation.
[212] A. S. Menon and L. Radom, J. Phys. Chem. A **112**, 13225 (2008).
[213] J. Baker, A. Scheiner, and J. Andzelm, Chem. Phys. Lett. **216**, 380 (1993).
[214] R. McWeeny and B. T. Sutcliffe, *Methods of Molecular Quantum Mechanics*, vol. 2 (Academic press, 1969).
[215] C. Roothaan, Rev. Mod. Phys. **32**, 179 (1960).
[216] N. Ferré, N. Guihéry, and J. P. Malrieu, Phys. Chem. Chem. Phys. **17**, 14375 (2015).
[217] T. Li, Z. J. Baum, and J. E. Goldberger, Eur. J. Inorg. Chem. **2016**, 28 (2016).
[218] X. Zhu and Y. Aoki, J. Comp. Chem. **36**, 1232 (2015).
[219] J. J. Eriksen, D. A. Matthews, P. Jørgensen, and J. Gauss,

J. Chem. Phys. **144**, 194102 (2016).
[220] Q. T. Tran and V. T. Tran, J. Chem. Phys. **144**, 214305, 1 (2016).
[221] M. C. Green, H. Nakata, D. G. Fedorov, and L. V. Slipchenko, Chem. Phys. Lett. **651**, 56 (2016).
[222] T. Jian, W. Li, I. A. Popov, G. V. Lopez, X. Chen, A. I. Boldyrev, J. Li, and L. Wang, J. Chem. Phys. **144**, 154310 (2016).
[223] B. Pamuk, J. Baima, R. Dovesi, M. Calandra, and F. Mauri, Phys. Rev. B **94**, 035101 (2016).
[224] P. B. C., V. Alsenoy, P. W. Ayers, and R. Carbó-Dorca, J. Chem. Phys. **126**, 144111 (2007).
[225] F. L. Hirshfeld, Theor Chim Acta **44**, 129 (1977).
[226] C. M. Zicovich-Wilson, A. M. Navarrete-López, M. Ho, and S. Casassa, J. Chem. Phys. **131**, 144101 (2009).
[227] T. C. Lillestolen and R. J. Wheatley, J. Chem. Phys. **131**, 144101 (2009).
[228] L. Maschio, B. Kirtman, R. Orlando, and M. Rérat, J. Chem. Phys. **137**, 204113 (2012).
[229] R. F. W. Bader, *Atoms in Molecules - A Quantum Theory* (Oxford University Press, Oxford, UK, 1990).
[230] M. F. Peintinger, D. V. Oliveira, and T. Bredow, J. Comput. Chem. **34**, 451 (2013).
[231] K. Parlinski, Z. Q. Li, and Y. Kawazoe, Phys. Rev. Lett. **78**, 4063 (1997).
[232] A. Togo, F. Oba, and I. Tanaka, Phys. Rev. B **78**, 134106 (2008).
[233] D. Alfè, Comp. Phys. Comm. **180**, 2622 (2009).
[234] A. Erba, M. Ferrabone, R. Orlando, and R. Dovesi, J. Comput. Chem. **34**, 346 (2013).
[235] J. Zhao, P. Gaskell, L. Cormier, and S. Bennington, Phys. B **241**, 906 (1997).
[236] R. Osborn, E. A. Goremychkin, A. I. Kolesnikov, and D. G. Hinks, Phys. Rev. Lett. **87**, 017005 (2001).
[237] M. S. Lucas, M. Kresch, R. Stevens, and B. Fultz, Phys. Rev. B **77**, 184303 (2008).
[238] V. Sears, Neutron News **3**, 29 (1992).
[239] B. S. Hudson, J. Phys. Chem. A **105**, 3949 (2001).
[240] A. O. Madsen, B. Civalleri, M. Ferrabone, F. Pascale, and A. Erba, Acta Crystallogr. Sec. A **69**, 309 (2013).
[241] T.-Y. Wu, Int. J. Theor. Phys. **2**, 325 (1969).
[242] G. K. H. Madsen and D. J. Singh, Comput. Phys. Comm. **175**, 67 (2006).
[243] G. Pizzi, D. Volja, B. Kozinsky, M. Fornari, and N. Marzari, Comput. Phys. Comm. **185**, 422 (2014).
[244] G. Sansone, A. Ferretti, and L. Maschio, J. Chem. Phys. **147**, 114101 (2017).
[245] J. K. Tomfhor and O. F. Sankey, Phys. Rev. B **65**, 245105 (2002).
[246] J. Tersoff, Phys. Rev. Lett. **52**, 465 (1984).
[247] A. Ferretti, B. Bonferroni, A. Calzolari, and M. B. Nardelli, *WANT code(2007)* (2007), http://www.wanniertransport.org.
[248] A. Ferretti, G. Mallia, L. Martin-Samos, G. Bussi, A. Ruini, B. Montanari, and N. M. Harrison, Phys. Rev. B **85**, 235105 (2012).